Simultaneous description of β decay and low-lying structure of neutron-rich even- and odd-mass Rh and Pd nuclei

Nomura, K.; Lotina, L.; Rodríguez-Guzmán, R.; Robledo, L. M.

Source / Izvornik: **Physical Review C, 2022, 106**

Journal article, Published version
Rad u časopisu, Objavljena verzija rada (izdavačev PDF)

https://doi.org/10.1103/PhysRevC.106.064304

PHYSICAL REVIEW C **106**, 064304 (2022)

Simultaneous description of β decay and low-lying structure of neutron-rich even- and odd-mass Rh and Pd nuclei

K. Nomura,[1,*] L. Lotina,[1] R. Rodríguez-Guzmán,[2] and L. M. Robledo[3,4]

[1]*Department of Physics, Faculty of Science, University of Zagreb, HR-10000 Zagreb, Croatia*
[2]*Departamento de Física Aplicada I, Escuela Politécnica Superior, Universidad de Sevilla, Seville, E-41011, Spain*
[3]*Departamento de Física Teórica and CIAFF, Universidad Autónoma de Madrid, E-28049 Madrid, Spain*
[4]*Center for Computational Simulation, Universidad Politécnica de Madrid, Campus de Montegancedo, Bohadilla del Monte, E-28660-Madrid, Spain*

(Received 6 September 2022; accepted 29 November 2022; published 7 December 2022)

The low-energy structure and β-decay properties of neutron-rich even- and odd-mass Pd and Rh nuclei are studied using a mapping framework based on the nuclear density-functional theory and the particle-boson coupling scheme. Constrained Hartree-Fock-Bogoliubov calculations using the Gogny-D1M energy density functional are performed to obtain microscopic inputs to determine the interacting-boson Hamiltonian employed to describe the even-even core Pd nuclei. The mean-field calculations also provide single-particle energies for the odd systems, which are used to determine essential ingredients of the particle-boson interactions for the odd-nucleon systems, and of the Gamow-Teller and Fermi transition operators. The potential-energy surfaces obtained for even-even Pd isotopes as well as the spectroscopic properties for the even- and odd-mass systems suggest a transition from prolate deformed to γ-unstable and to nearly spherical shapes. The predicted β-decay $\log ft$ values are shown to be sensitive to the details of the wave functions for the parent and daughter nuclei and therefore serve as a stringent test of the employed theoretical approach.

DOI: 10.1103/PhysRevC.106.064304

I. INTRODUCTION

Precise measurements and theoretical descriptions associated with the low-energy nuclear structure are crucial to the accurate modeling and better understanding of fundamental nuclear processes, such as β and double-β ($\beta\beta$) decays intimately connected to stellar nucleosynthesis. In this context, the low-energy excitations and decay properties of neutron-rich nuclei with mass $A \approx 100$ and neutron number $N \approx 60$ are of particular interest from both the nuclear structure and astrophysical points of view. Those nuclei exhibit a rich variety of phenomena such as shell evolution, onset of collectivity, quantum (shape) phase transitions and shape coexistence. They are also involved in the rapid neutron-capture (r) process responsible for the nucleosynthesis of heavy chemical elements in explosive environments.

The β decay half-lives of heavy neutron-rich nuclei have been extensively measured using radioactive-ion beams at major experimental facilities around the world. For example, the neutron-rich $A \approx 110$ nuclei from Kr to Tc [1], and from Rb to Sn [2] have been studied at the RIBF facility at RIKEN. The $A \approx 90$ region from Se to Zr isotopic chains has been studied at the NSCL at MSU [3]. Moreover, several $A \approx$ 100–110 nuclei are of special interest, including ^{96}Zr, ^{96}Mo, ^{100}Mo, ^{100}Ru, ^{110}Pd, and ^{110}Cd, since they correspond to the parent or daughter nuclei for the possible neutrinoless $\beta\beta$ decays [4].

From a theoretical point of view, the consistent description of both low-lying nuclear states and β-decay properties represents a major challenge. Theoretical studies of the β-decay process have been carried out within the interacting boson model (IBM) [5–14], the quasiparticle random-phase approximation (QRPA) [15–23], and the large-scale shell model (LSSM) [24–28]. The calculation of β-decay properties serves as a stringent test of a given theoretical approach, since the decay rate of this process is very sensitive to the structure of the wave functions corresponding to the low-energy states of both the parent and daughter nuclei.

In this paper, we present a simultaneous description of the low-energy collective excitations and β-decay properties of even- and odd-A neutron-rich Pd and Rh isotopes in the mass range $A \approx$ 100–120. They represent a region of interest for future experiments and for astrophysical applications. Calculations are performed within a theoretical framework based on the nuclear density-functional theory and the particle-core coupling scheme. In it even-even nuclei are described using the IBM [29]. The particle-core couplings for the odd-mass, and odd-odd nuclei are described using the interacting boson-fermion model (IBFM) [30,31] and the interacting boson-fermion-fermion model (IBFFM) [31,32], respectively. The bosonic-core Hamiltonian is built using microscopic input from self-consistent Hartree-Fock-Bogoliubov (HFB) [33] calculations based on the parametrization D1M [34] of the Gogny energy density functional (EDF) [35,36]. Essential building blocks of the particle-boson interactions and of the Gamow-Teller (GT) and Fermi (F) transition operators for the β decay are also determined with the aid of the same

---

[*] knomura@phy.hr

Gogny-EDF results. The method has already been applied to study the shape evolution and β decay properties of the odd-A [11] and even-A [12] nuclei in the mass $A \approx 130$ region. It has also been employed to study even- and odd-A As and Ge nuclei in the $A \approx 70$–80 region using microscopic input from relativistic Hartree-Bogoliubov calculations, based on the density-dependent point-coupling interaction [14].

The main goal of this work is to examine the performance of the method mentioned above in the case of neutron-rich nuclei, including those for which experimental information is scarce. The results to be discussed latter on in the paper also illustrate the predictive power of the EDF-based IBM to describe the low-lying structure and β decay in this region of the nuclear chart where future experiments are expected. To identify the relevance of the low-lying structures of individual nuclei in the β decay, we perform a detailed analysis of the wave functions obtained for both the parent and daughter nuclei of the decay. In addition, we perform conventional IBM calculations, with the parameters for the even-even boson core Hamiltonians taken from the earlier phenomenological calculation [37]. The corresponding results are compared with those from the EDF-based IBM calculations. Note that the present study is restricted to both types of allowed β decays, i.e., the transition conserves parity and takes place between states that differ in the total angular momentum I by $\Delta I = 0$ or 1.

To support our choice we note that, like other nonrelativistic [38] and relativistic [39,40] EDFs, theoretical approaches based on the parametrizations D1M and D1S [41] of the Gogny-EDF both at the mean-field level and beyond have been extensively employed to study the low-energy nuclear structure and dynamics in various regions of the nuclear chart as well as fundamental nuclear processes (see Ref. [36] for a review and references therein). In particular spectroscopic studies involving collective degrees of freedom have been carried out within the symmetry-projected generator coordinate method (GCM) [33] using the Gogny forces and involving different levels of sophistication [36,42–48]. Furthermore, the mapping procedure leading to an IBM Hamiltonian from microscopic Gogny mean-field input has already shown its ability to describe spectroscopic properties associated with shape phase transitions, shape coexistence, and octupole deformations in nuclei [49–56].

The paper is organized as follows: The theoretical framework is briefly outlined in Sec. II. The excitation spectra and electromagnetic transition properties obtained for even-even Pd (Sec. III), odd-A Pd and Rh (Sec. IV), and odd-odd Rh nuclei (Sec. V) are discussed. The computed $\log ft$ values for the β decays of the odd- and even-A Rh into Pd nuclei are discussed in detail in Sec. VI. Finally, Sec. VII is devoted to the concluding remarks.

II. THEORETICAL FRAMEWORK

In this section, we describe the particle-core Hamiltonian (Sec. II A), and the procedure to build it (Sec. II B). Electromagnetic transition operators are discussed in Sec. II C, and Gamow-Teller and Fermi operators are introduced in Sec. II D.

A. Particle-core Hamiltonian

In this study, we use the neutron-proton IBM (IBM-2) [57,58]. In this model both neutron and proton monopole (s_ν and s_π), and quadrupole (d_ν and d_π) bosons are considered as fundamental degrees of freedom. From a microscopic point of view [57,58], the s_ν (s_π) and d_ν (d_π) bosons are associated with the collective S_ν (S_π) and D_ν (D_π) pairs of valence neutrons (protons) with angular momenta and parity 0^+ and 2^+, respectively. In comparison with the simpler IBM-1, in which the neutrons and protons are not distinguished, the IBM-2 appears to be more suitable to treat β decay, since in this process both proton and neutron degrees of freedom should be explicitly taken into account. For the model space the neutron $N = 50$–82 and proton $Z = 28$–50 major shells are used. Hence for $^{104-124}$Pd, the number of neutron bosons, N_ν, varies within the range $2 \leqslant N_\nu \leqslant 8$, while the number of the proton bosons is fixed, $N_\pi = 2$.

To deal with even-even, odd-mass, and odd-odd nuclei on an equal footing, both collective and single-particle degrees of freedom are treated within the framework of the neutron-proton IBFFM (IBFFM-2). The IBFFM-2 Hamiltonian reads

$$\hat{H} = \hat{H}_{\mathrm{B}} + \hat{H}_{\mathrm{F}}^{\nu} + \hat{H}_{\mathrm{F}}^{\pi} + \hat{V}_{\mathrm{BF}}^{\nu} + \hat{V}_{\mathrm{BF}}^{\pi} + \hat{V}_{\nu\pi}, \tag{1}$$

where $\hat{H}_{\mathrm{B}}$ is the IBM-2 Hamiltonian representing the bosonic even-even core, $\hat{H}_{\mathrm{F}}^{\nu}$ ($\hat{H}_{\mathrm{F}}^{\pi}$) is the one-body, single-neutron (-proton) Hamiltonian, and $\hat{V}_{\mathrm{BF}}^{\nu}$ ($\hat{V}_{\mathrm{BF}}^{\pi}$) stands for the interaction between the odd neutron (proton) and the even-even IBM-2 core. The last term $\hat{V}_{\nu\pi}$ represents the residual interaction between the odd neutron and the odd proton.

The IBM-2 Hamiltonian takes the form

$$\hat{H}_{\mathrm{B}} = \epsilon_d(\hat{n}_{d_\nu} + \hat{n}_{d_\pi}) + \kappa\hat{Q}_\nu \cdot \hat{Q}_\pi, \tag{2}$$

where in the first term, $\hat{n}_{d_\rho} = d_\rho^\dagger \cdot \tilde{d}_\rho$ ($\rho = \nu$ or π) is the d-boson number operator, with ϵ_d the single d-boson energy relative to the s-boson one, and $\tilde{d}_{\rho\mu} = (-1)^\mu d_{\rho-\mu}$. The second term stands for the quadrupole-quadrupole interaction between neutron and proton boson systems with strength κ, and $\hat{Q}_\rho = d_\rho^\dagger s_\rho + s_\rho^\dagger \tilde{d}_\rho + \chi_\rho(d_\rho^\dagger \times \tilde{d}_\rho)^{(2)}$ represents the bosonic quadrupole operator, with the dimensionless parameter χ_ρ.

The single-nucleon Hamiltonian $\hat{H}_{\mathrm{F}}^{\rho}$ takes the form

$$\hat{H}_{\mathrm{F}}^{\rho} = -\sum_{j_\rho} \epsilon_{j_\rho} \sqrt{2j_\rho + 1}\left(a_{j_\rho}^\dagger \times \tilde{a}_{j_\rho}\right)^{(0)}, \tag{3}$$

where ϵ_{j_ρ} stands for the single-particle energy of the odd neutron ($\rho = \nu$) or proton ($\rho = \pi$) orbital j_ρ. a_{j_ρ} and $a_{j_\rho}^\dagger$ are annihilation and creation operators of the single particle, respectively. The operator $\tilde{a}_{j_\rho}$ is defined as $\tilde{a}_{j_\rho m_\rho} = (-1)^{j_\rho - m_\rho} a_{j_\rho - m_\rho}$.

In this study, we employ the following boson-fermion interaction $\hat{V}_{\mathrm{BF}}^{\rho}$ [31]

$$\hat{V}_{\mathrm{BF}}^{\rho} = \Gamma_\rho \hat{V}_{\mathrm{dyn}}^{\rho} + \Lambda_\rho \hat{V}_{\mathrm{exc}}^{\rho} + A_\rho \hat{V}_{\mathrm{mon}}^{\rho}. \tag{4}$$

The first, second, and third terms are dynamical quadrupole, exchange, and monopole interactions, respectively. Within the generalized seniority scheme [31,59], the dynamical and exchange terms are assumed to be dominated by the interaction

TABLE I. Even-even Pd core, and the neighboring odd-N Pd, odd-Z Rh, and odd-odd Rh nuclei considered in this study.

Even-even core	Odd-N	Odd-Z	Odd-odd
${}^{A}_{46}\mathrm{Pd}_{N}$ ($58 \leqslant N \leqslant 64$)	${}^{A+1}_{46}\mathrm{Pd}_{N+1}$	${}^{A-1}_{45}\mathrm{Rh}_{N}$	${}^{A}_{45}\mathrm{Rh}_{N+1}$
${}^{112}_{46}\mathrm{Pd}_{66}$		${}^{111}_{45}\mathrm{Rh}_{66}$	
${}^{A}_{46}\mathrm{Pd}_{N}$ ($68 \leqslant N \leqslant 78$)	${}^{A-1}_{46}\mathrm{Pd}_{N-1}$	${}^{A-1}_{45}\mathrm{Rh}_{N}$	${}^{A-2}_{45}\mathrm{Rh}_{N-1}$

between unlike particles. On the other hand, the monopole term is assumed to be dominated by the interaction between like particles. The explicit form of the different terms in Eq. (4) then read

$$\hat{V}^{\rho}_{\mathrm{dyn}} = \sum_{j_\rho j'_\rho} \gamma_{j_\rho j'_\rho} \left(a^\dagger_{j_\rho} \times \tilde{a}_{j'_\rho}\right)^{(2)} \cdot \hat{Q}_{\rho'}, \tag{5}$$

$$\hat{V}^{\rho}_{\mathrm{exc}} = -(s^\dagger_{\rho'} \times \tilde{d}_{\rho'})^{(2)} \cdot \sum_{j_\rho j'_\rho j''_\rho} \sqrt{\frac{10}{N_\rho(2j_\rho+1)}} \beta_{j_\rho j'_\rho} \beta_{j''_\rho j_\rho}$$

$$: \left(\left(d^\dagger_\rho \times \tilde{a}_{j''_\rho}\right)^{(j_\rho)} \times \left(a^\dagger_{j'_\rho} \times \tilde{s}_\rho\right)^{(j'_\rho)}\right)^{(2)} : +(\mathrm{H.c.}), \tag{6}$$

$$\hat{V}^{\rho}_{\mathrm{mon}} = -\hat{n}_{d_\rho} \sum_{j_\rho} \sqrt{2j_\rho+1} (a^\dagger_{j_\rho} \times \tilde{a}_{j_\rho})^{(0)}, \tag{7}$$

where the coefficients $\gamma_{j_\rho j'_\rho} = (u_{j_\rho} u_{j'_\rho} - v_{j_\rho} v_{j'_\rho}) Q_{j_\rho j'_\rho}$, and $\beta_{j_\rho j'_\rho} = (u_{j_\rho} v_{j'_\rho} + v_{j_\rho} u_{j'_\rho}) Q_{j_\rho j'_\rho}$ are proportional to the matrix elements of the fermion quadrupole operator in the single-particle basis $Q_{j_\rho j'_\rho} = \langle \ell_\rho \frac{1}{2} j_\rho \| Y^{(2)} \| \ell'_\rho \frac{1}{2} j'_\rho \rangle$. The operator $\hat{Q}_{\rho'}$ in Eq. (5) is the same boson quadrupole operator as in the boson Hamiltonian (2). In Eq. (6) the notation $: (\cdots) :$ stands for normal ordering. Within this formalism, the single-particle energy ϵ_{j_ρ} in Eq. (3) is replaced with the quasiparticle energy $\tilde{\epsilon}_{j_\rho}$.

For the residual neutron-proton interaction $\hat{V}_{\nu\pi}$ in Eq. (1), we adopt the form [60]

$$\hat{V}_{\nu\pi} = 4\pi v_{\mathrm{d}} \delta(\boldsymbol{r}) \delta(\boldsymbol{r}_\nu - r_0) \delta(\boldsymbol{r}_\pi - r_0) + v_{\mathrm{t}} \left[\frac{3(\boldsymbol{\sigma}_\nu \cdot \mathbf{r})(\boldsymbol{\sigma}_\pi \cdot \mathbf{r})}{r^2} - \boldsymbol{\sigma}_\nu \cdot \boldsymbol{\sigma}_\pi \right], \tag{8}$$

where the first and second terms are surface-delta and tensor interactions with strength parameters v_{d}, and v_{t}, respectively. Note that $\boldsymbol{r} = \boldsymbol{r}_\nu - \boldsymbol{r}_\pi$ and $r_0 = 1.2A^{1/3}$ fm.

Table I summarizes the even-even Pd core nuclei, neighboring odd-A Pd and Rh, and odd-odd Rh nuclei considered in this study.

B. Procedure to build the Hamiltonian

In the initial step a set of constrained HFB calculations for even-even Pd isotopes based on the parametrization D1M of the Gogny-EDF is carried out to obtain the microscopic input to build the IBFFM-2 Hamiltonian. For each even-even Pd isotope, those calculations provide the corresponding energy surfaces, i.e., the total mean-field energies as functions of the triaxial quadrupole deformations β and γ [61]. For each nucleus, the Gogny-D1M HFB energy surface is mapped onto the expectation value of the IBM-2 Hamiltonian $\hat{H}_{\mathrm{B}}$ (2) in the boson condensate state [62]. This procedure specifies the parameters of the boson Hamiltonian, i.e., ϵ_d, κ, χ_ν, and χ_π. For more details about the mapping procedure, the reader is referred to Refs. [63,64].

Next, the Hamiltonian $\hat{H}_{\mathrm{F}}$ of Eq. (3) and the boson-fermion interactions $\hat{V}_{\mathrm{BF}}$ of Eq. (4) are determined using the procedure of Refs. [65,66]. The single-particle energies ϵ_{j_ρ} of the odd nucleon are obtained from HFB calculations constrained to zero quadrupole deformation. Once the single-particle energies are available, the quasiparticle energies $\tilde{\epsilon}_{j_\rho}$ and occupation probabilities $v^2_{j_\rho}$ are computed within the BCS approximation, separately for neutron and proton single-particle spaces. The empirical pairing gap $12A^{-1/2}$ is used. We include in the BCS calculations the $2s_{1/2}$, $1d_{3/2}$, $1d_{5/2}$, $0g_{7/2}$, $0g_{9/2}$, and $0h_{11/2}$ orbitals for the odd neutron, and the $1d_{5/2}$, $0g_{7/2}$, $0g_{9/2}$, $2p_{1/2}$, $2p_{3/2}$, and $1f_{5/2}$ orbitals for the odd proton. The corresponding quasiparticle energies $\tilde{\epsilon}_{j_\nu}$ ($\tilde{\epsilon}_{j_\pi}$), and occupation probabilities $v^2_{j_\nu}$ ($v^2_{j_\pi}$) for the odd neutron (proton) $2s_{1/2}$, $1d_{3/2}$, $1d_{5/2}$, and $0g_{7/2}$ ($1d_{5/2}$, $0g_{7/2}$, and $0g_{9/2}$) orbitals are taken as the inputs to $\hat{H}^{\nu}_{\mathrm{F}}$ ($\hat{H}^{\pi}_{\mathrm{F}}$) and $\hat{V}^{\nu}_{\mathrm{BF}}$ ($\hat{V}^{\pi}_{\mathrm{BF}}$), respectively. The strength parameters Γ_ρ, Λ_ρ, and A_ρ for $\hat{V}^{\rho}_{\mathrm{BF}}$ are then fixed so that the observed low-energy positive-parity levels for the odd-A Pd ($\rho = \nu$) or odd-Z Rh ($\rho = \pi$) nuclei are reproduced reasonably well.

Finally, the parameters v_{d} and v_{t} for the residual neutron-proton interaction in Eq. (8) are determined [67] so that the observed low-lying positive-parity states for each odd-odd Rh nucleus are reasonably well reproduced. Note that the same strength parameters as those obtained in the previous step for the neighboring odd-A nuclei are employed in the IBFFM-2 calculations for odd-odd nuclei. On the other hand, the quasiparticle energies and occupation probabilities of the odd particles are independently computed.

Figure 1 shows the neutron and proton spherical single-particle energies (ϵ_{j_ν} and ϵ_{j_π}), resulting from the Gogny-HFB calculations, and the quasiparticle energies ($\tilde{\epsilon}_{j_\nu}$ and $\tilde{\epsilon}_{j_\pi}$) and occupation probabilities ($v^2_{j_\nu}$ and $v^2_{j_\pi}$) used in the IBFM-2 and IBFFM-2 calculations.

C. Electromagnetic transition operators

Theories with effective degrees of freedom, like the IBFFM, require the definition of transition operators to be used in the evaluation of electromagnetic transition probabilities. For the electric $E2$ transition the operator $\hat{T}^{(E2)}$ to be used in the IBFFM-2 takes the form [31]

$$\hat{T}^{(E2)} = \hat{T}^{(E2)}_{\mathrm{B}} + \hat{T}^{(E2)}_{\mathrm{F}}, \tag{9}$$

where the first and second terms are the boson and fermion parts, respectively. They are given by

$$\hat{T}^{(E2)}_{\mathrm{B}} = \sum_{\rho=\nu,\pi} e^{\mathrm{B}}_{\rho} \hat{Q}_\rho, \tag{10}$$

and

$$\hat{T}^{(E2)}_{\mathrm{F}} = -\frac{1}{\sqrt{5}} \sum_{\rho=\nu,\pi} \sum_{j_\rho j'_\rho} \left(u_{j_\rho} u_{j'_\rho} - v_{j_\rho} v_{j'_\rho}\right) \times \left\langle \ell_\rho \frac{1}{2} j_\rho \middle\| e^{\mathrm{F}}_\rho r^2 Y^{(2)} \middle\| \ell'_\rho \frac{1}{2} j'_\rho \right\rangle \left(a^\dagger_{j_\rho} \times \tilde{a}_{j'_\rho}\right)^{(2)}. \tag{11}$$

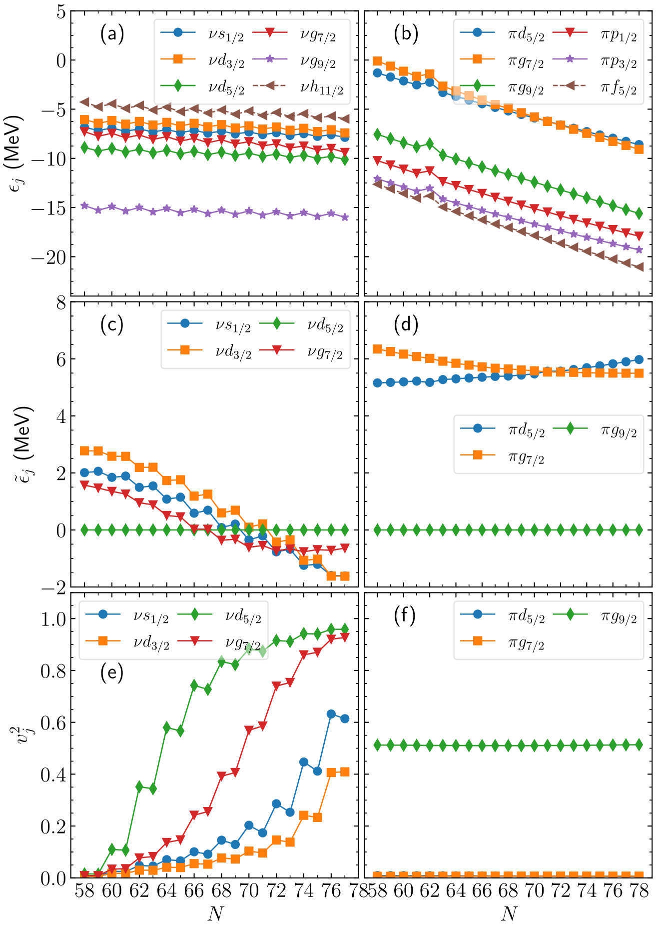

FIG. 1. (a), (b) The single-particle energies ϵ_{j_ρ}, obtained from the Gogny-D1M HFB calculations at the spherical configuration, (c), (d) the quasiparticle energies $\tilde{\epsilon}_{j_\rho}$, and (e), (f) the occupation probabilities $v^2_{j_\rho}$, obtained from the BCS calculations. Results shown in the left column are for the odd neutron in the odd-*A* Pd and even-*A* Rh nuclei, and those in the right column are for the odd proton in the even- and odd-*A* Rh nuclei.

The fixed values $e^{\rm B}_\nu = e^{\rm B}_\pi = 0.1\ e\,$b for the boson effective charges are taken so that the experimental $B(E2; 2^+_1 \to 0^+_1)$ transition probabilities are reproduced for even-even Pd isotopes. The standard neutron and proton effective charges $e^{\rm F}_\nu = 0.5\ e\,$b, $e^{\rm F}_\pi = 1.5\ e\,$b are employed for all the studied odd-nucleon systems. The $M1$ transition operator $\hat{T}^{(M1)}$ is defined as

$$\hat{T}^{(M1)} = \sqrt{\frac{3}{4\pi}} \sum_{\rho=\nu,\pi} \Bigg[g^{\rm B}_\rho \hat{L}_\rho - \frac{1}{\sqrt{3}} \sum_{j_\rho j'_\rho} (u_{j_\rho} u_{j'_\rho} + v_{j_\rho} v_{j'_\rho}) \times \langle j_\rho \| g^\rho_l \mathbf{l} + g^\rho_s \mathbf{s} \| j'_\rho \rangle \big(a^\dagger_{j_\rho} \times \tilde{a}_{j'_\rho}\big)^{(1)} \Bigg]. \tag{12}$$

The empirical g factors $g^{\rm B}_\nu = 0\ \mu_N$ (nuclear magneton) and $g^{\rm B}_\pi = 1.0\ \mu_N$, are adopted for the neutron and proton bosons. For the neutron (proton) g factors, the standard Schmidt values $g^\nu_l = 0\,\mu_N$ and $g^\nu_s = -3.82\ \mu_N$ ($g^\pi_l = 1.0\ \mu_N$ and $g^\pi_s = 5.58\ \mu_N$) are used, with g^ρ_s quenched by 30% with respect to the free value.

D. Gamow-Teller and Fermi transition operators

As in the electromagnetic case, the transition operators for allowed β decay have to be redefined in terms of the relevant degrees of freedom of the model. The Gamow-Teller $\hat{T}^{\rm GT}$ and Fermi $\hat{T}^{\rm F}$ transition operators take the form

$$\hat{T}^{\rm GT} = \sum_{j_\nu j_\pi} \eta^{\rm GT}_{j_\nu j_\pi} \big(\hat{P}_{j_\nu} \times \hat{P}_{j_\pi}\big)^{(1)}, \tag{13}$$

$$\hat{T}^{\rm F} = \sum_{j_\nu j_\pi} \eta^{\rm F}_{j_\nu j_\pi} \big(\hat{P}_{j_\nu} \times \hat{P}_{j_\pi}\big)^{(0)}, \tag{14}$$

with the coefficients

$$\eta^{\rm GT}_{j_\nu j_\pi} = -\frac{1}{\sqrt{3}} \left\langle \ell_\nu \frac{1}{2} j_\nu \middle\| \boldsymbol{\sigma} \middle\| \ell_\pi \frac{1}{2} j_\pi \right\rangle \delta_{\ell_\nu \ell_\pi}, \tag{15}$$

$$\eta^{\rm F}_{j_\nu j_\pi} = -\sqrt{2j_\nu + 1}\,\delta_{j_\nu j_\pi}. \tag{16}$$

In Eqs. (13) and (14), $\hat{P}_{j_\rho}$ represents one of the one-particle creation operators

$$A^\dagger_{j_\rho m_\rho} = \zeta_{j_\rho} a^\dagger_{j_\rho m_\rho} + \sum_{j'_\rho} \zeta_{j_\rho j'_\rho} s^\dagger_\rho \Big(\tilde{d}_\rho \times a^\dagger_{j'_\rho}\Big)^{(j_\rho)}_{m_\rho}, \tag{17a}$$

$$B^\dagger_{j_\rho m_\rho} = \theta_{j_\rho} s^\dagger_\rho \tilde{a}_{j_\rho m_\rho} + \sum_{j'_\rho} \theta_{j_\rho j'_\rho} \Big(d^\dagger_\rho \times \tilde{a}_{j'_\rho}\Big)^{(j_\rho)}_{m_\rho}, \tag{17b}$$

and the annihilation operators

$$\tilde{A}_{j_\rho m_\rho} = (-1)^{j_\rho - m_\rho} A_{j_\rho - m_\rho}, \tag{17c}$$

$$\tilde{B}_{j_\rho m_\rho} = (-1)^{j_\rho - m_\rho} B_{j_\rho - m_\rho}. \tag{17d}$$

The operators in Eqs. (17a) and (17c) conserve the boson number, whereas those in Eqs. (17b) and (17d) do not. The operators $\hat{T}^{\rm GT}$ and $\hat{T}^{\rm F}$ are expressed as a combination of two of the operators in Eqs. (17a)–(17d), depending on the type of the β decay studied (i.e., β^+ or β^-) and on the particle or hole nature of the valence nucleons. In the present case,

$$\hat{P}_{j_\nu} = \begin{cases} \tilde{B}_{j_\nu, m_\nu} & (N \leqslant 66) \\ \tilde{A}^\dagger_{j_\nu, m_\nu} & (N \geqslant 68) \end{cases} \tag{18}$$

for the β^- decay of the odd-*A* Rh, while

$$\hat{P}_{j_\nu} = \begin{cases} \tilde{A}_{j_\nu, m_\nu} & (N \leqslant 65) \\ \tilde{B}^\dagger_{j_\nu, m_\nu} & (N \geqslant 67) \end{cases} \tag{19}$$

for the β^- decay of the even-*A* Rh. On the other hand, $\hat{P}_{j_\pi} = \tilde{A}_{j_\pi, m_\pi}$ for all the considered β^- decays. Note that Eqs. (17a)–(17d) are simplified forms of the most general one-particle transfer operators in the IBFM-2 [31].

By using the generalized seniority scheme, the coefficients ζ_j, $\zeta_{jj'}$, θ_j, and $\theta_{jj'}$ in Eqs. (17a) and (17b) can be written as [68]

$$\zeta_{j_\rho} = u_{j_\rho} \frac{1}{K'_{j_\rho}}, \tag{20a}$$

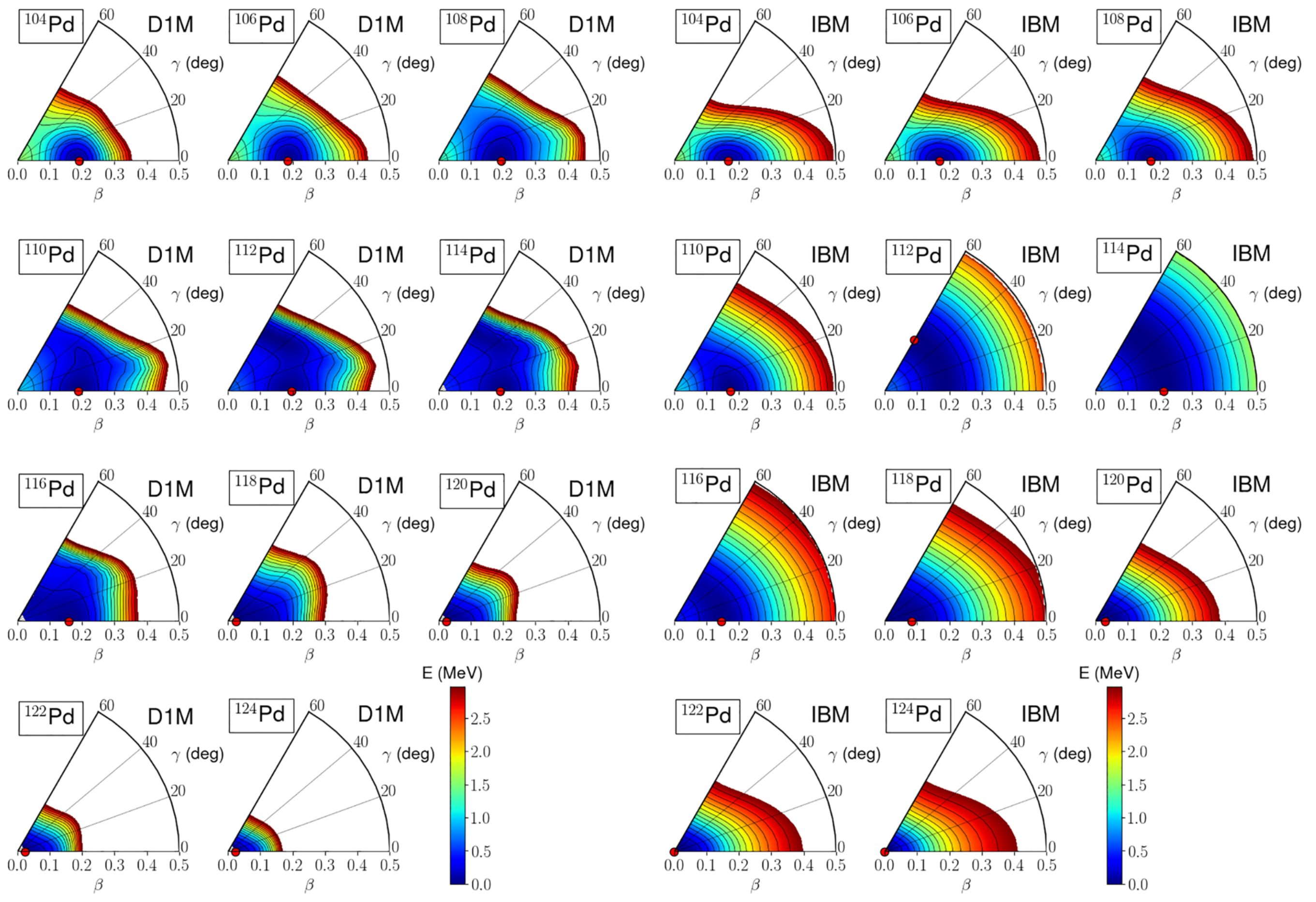

FIG. 2. The Gogny-D1M HFB and mapped IBM-2 potential-energy surfaces as functions of the (β, γ) deformation parameters for the even-even $^{104-124}$Pd nuclei. The energy difference between neighboring contours is 200 keV. The global minimum is identified by a solid circle.

$$\zeta_{j_\rho j'_\rho} = -v_{j_\rho}\beta_{j'_\rho j_\rho}\sqrt{\frac{10}{N_\rho(2j_\rho+1)}}\frac{1}{KK'_{j_\rho}}, \tag{20b}$$

$$\theta_{j_\rho} = \frac{v_{j_\rho}}{\sqrt{N_\rho}}\frac{1}{K''_{j_\rho}}, \tag{20c}$$

$$\theta_{j_\rho j'_\rho} = u_{j_\rho}\beta_{j'_\rho j_\rho}\sqrt{\frac{10}{2j_\rho+1}}\frac{1}{KK''_{j_\rho}}. \tag{20d}$$

The factors K, K'_{j_ρ}, and K''_{j_ρ} are defined as

$$K = \left(\sum_{j_\rho j'_\rho}\beta^2_{j_\rho j'_\rho}\right)^{1/2}, \tag{21a}$$

$$K'_{j_\rho} = \left[1 + 2\left(\frac{v_{j_\rho}}{u_{j_\rho}}\right)^2 \frac{\langle(\hat{n}_{s_\rho}+1)\hat{n}_{d_\rho}\rangle_{0^+_1}}{N_\rho(2j_\rho+1)}\frac{\sum_{j'_\rho}\beta^2_{j'_\rho j_\rho}}{K^2}\right]^{1/2}, \tag{21b}$$

$$K''_{j_\rho} = \left[\frac{\langle\hat{n}_{s_\rho}\rangle_{0^+_1}}{N_\rho} + 2\left(\frac{u_{j_\rho}}{v_{j_\rho}}\right)^2 \frac{\langle\hat{n}_{d_\rho}\rangle_{0^+_1}}{2j_\rho+1}\frac{\sum_{j'_\rho}\beta^2_{j'_\rho j_\rho}}{K^2}\right]^{1/2}, \tag{21c}$$

where $\hat{n}_{s_\rho}$ is the number operator for the s_ρ boson and $\langle\cdots\rangle_{0^+_1}$ stands for the expectation value of a given operator in the 0^+_1 ground state of the even-even nucleus. The amplitudes v_{j_ρ} and u_{j_ρ} appearing in Eqs. (20a)–(20d) and (21a)–(21c) are the same as those used in the IBFM-2 (or IBFFM-2) calculations for the odd-mass (or odd-odd) nuclei. No additional parameter is introduced for the GT and Fermi operators. For a more detailed account on β-decay operators within the IBFM-2 or IBFFM-2 framework, the reader is also referred to Refs. [6,31,68].

The β-decay ft values are given by

$$ft = \frac{K}{|M(\mathrm{F})|^2 + \left(\frac{g_A}{g_V}\right)^2|M(\mathrm{GT})|^2}, \tag{22}$$

where the numeric constant K takes the value $K = 6163$ s. The quantities $M(\mathrm{F})$ and $M(\mathrm{GT})$ are the reduced matrix elements of the operators $\hat{T}^{\mathrm{F}}$ of Eq. (14) and $\hat{T}^{\mathrm{GT}}$ of Eq. (13), respectively. Here g_{V} and g_{A} are the vector and axial-vector coupling constants, respectively. In this study, we use the free nucleon values, $g_{\mathrm{V}} = 1$ and $g_{\mathrm{A}} = 1.27$, for the β decays of both even- and odd-A Rh.

III. EVEN-EVEN NUCLEI

A. Potential-energy surfaces

The Gogny-D1M HFB and mapped IBM-2 potential-energy surfaces are shown in Fig. 2 as functions of the (β, γ) deformation parameters for the even-even $^{104–124}$Pd nuclei. The variation of the HFB potential-energy surfaces as functions of the neutron number suggests a transition from prolate (for $N \lesssim 62$) to γ-soft ($64 \lesssim N \lesssim 70$), and to nearly spherical ($N \gtrsim 72$) shapes. In particular, both ^{112,114}Pd exhibit rather flat potential-energy surfaces along the γ direction. This is what is expected in the γ-unstable O(6) limit of the IBM [29]. In the case of ^{116}Pd, a flat-bottomed potential with a weak γ dependence, characteristic of the E(5) critical-point symmetry [69], is obtained.

For each of the considered nuclei, the Gogny-HFB and IBM-2 energy surfaces display a similar topology in the neighborhood of the global minimum (the location of the minimum, and the softness in the β and γ directions are similar). However, the mapped IBM-2 surfaces generally become flat at large β deformation ($\beta \gtrsim 0.4$). This difference is a consequence of the fact that in the HFB approach all nucleonic degrees of freedom are taken into account while the IBM-2 is built on the more limited model (valence) space of nucleon pairs. However, since the mean-field configurations most relevant to the low-energy collective excitations are those in the vicinity of the global minimum, the mapping is considered specifically in that region [63,64].

B. Spectroscopic properties

The mapped IBM-2 excitation energies of the 2_1^+, 4_1^+, 0_2^+, and 2_2^+ states in the even-even $^{104–124}$Pd nuclei are shown in Fig. 3 as functions of the neutron number N. Results obtained using the conventional IBM-2 approach (hereinafter referred to as phenomenological IBM-2), with parameters adopted from the earlier phenomenological study [37], are also included in the plot. As can be seen from the figure, the excitation energies decrease toward the middle of the major shell, i.e., $N = 66$. For $N \leqslant 64$, the mapped IBM-22_1^+ and 4_1^+ excitation energies underestimate the experimental ones while the energies of the non-yrast 0_2^+ and 2_2^+ states are overestimated. In the mapped (phenomenological) IBM-2 approach the ratios $R_{4/2}$ of the 4_1^+ to 2_1^+ excitation energies are 2.96 (2.43), 2.86 (2.39), and 2.69 (2.34) for ^{104}Pd, ^{106}Pd, and ^{108}Pd, respectively. These values should be compared with the experimental ratios of 2.38, 2.40, and 2.41. Thus, the mapped IBM-2 provides excitation spectra which are more rotational in character than the phenomenological IBM-2 and experimental ones. Around the neutron midshell $N = 66$, both the predicted and experimental 2_2^+ levels have the lowest energies, being even below the 4_1^+ state. The 2_2^+ state is the bandhead of the quasi-γ band, and the lowering of this state reflects an emergence of pronounced γ softness.

The IBM-2 parameters obtained for the even-even Pd isotopes from the mapping procedure, and those determined phenomenologically are shown in Fig. 4. The phenomenological IBM-2 parameters are extracted from earlier fitting calculations for Pd and Ru isotopes [37]. In Ref. [37], in

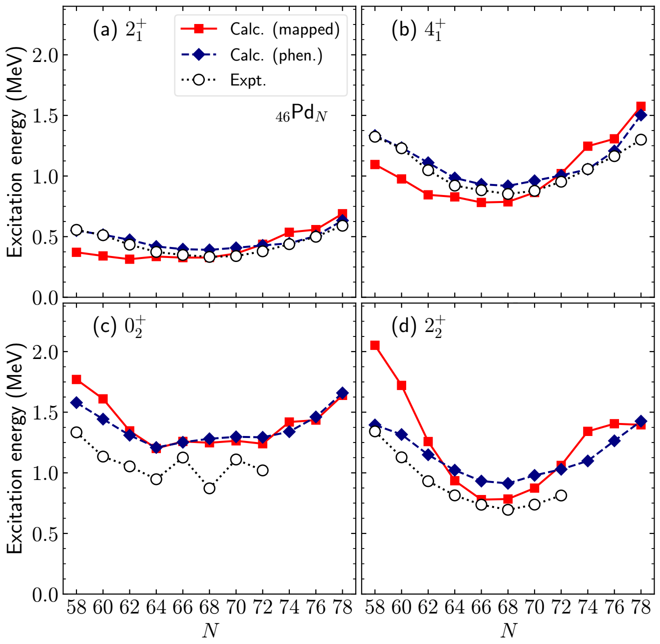

FIG. 3. Excitation energies of the (a) 2_1^+, (b) 4_1^+, (c) 0_2^+, and (d) 2_2^+ states in the even-even $^{104–124}$Pd nuclei. Results are obtained within the mapped and phenomenological (Phen.) IBM-2. Experimental data are taken from Ref. [70].

addition to the terms that appear in Eq. (2), the like-boson interactions, and the so-called Majorana terms were included in the model Hamiltonian. These terms were, however, shown to play a minor role [37], and are omitted in the present study. From Fig. 4, one sees that the single-d boson energy ϵ_d and

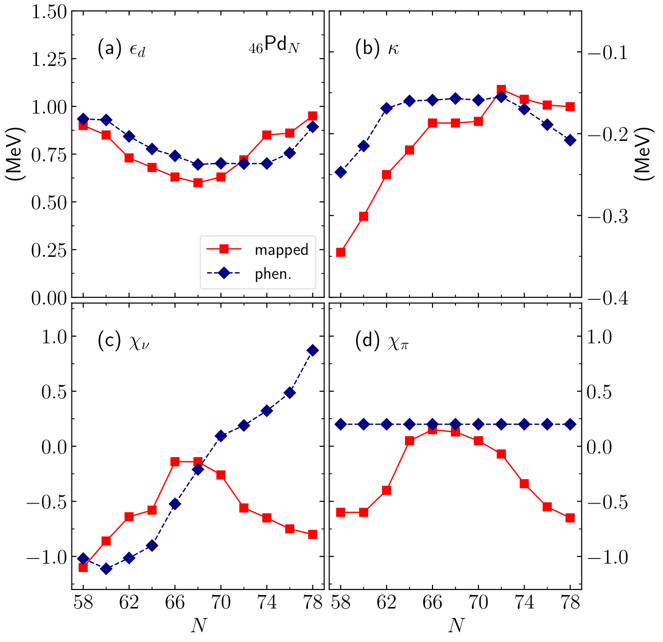

FIG. 4. Parameters for the even-even boson-core Hamiltonian (2) employed in the mapped and phenomenological (Phen.) IBM-2 calculations for even-even Pd isotopes.

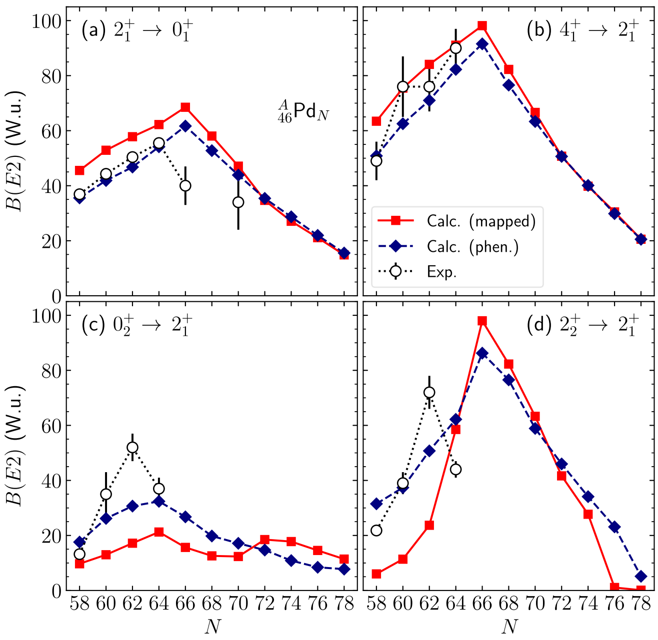

FIG. 5. The reduced transition probabilities $B(E2)$ for the transitions (a) $2_1^+ \to 0_1^+$, (b) $4_1^+ \to 2_1^+$, (c) $0_2^+ \to 2_1^+$, and (d) $2_2^+ \to 2_1^+$ in even-even Pd isotopes in comparison with the experimental data [70].

the strength κ have similar nucleon-number dependence for both the mapped and phenomenological IBM-2 models. A notable quantitative difference is that the derived κ values for the former are ≈1.4 larger in magnitude than for the latter. The behavior of the parameter χ_ν is different in the two approaches for $N \geqslant 70$. The sign and absolute value of the sum $\chi_\nu + \chi_\pi$ reflect the extent of γ softness and whether the nucleus is prolate or oblate deformed. In both calculations, the sum is negative, $\chi_\nu + \chi_\pi < 0$, for $N \lesssim 64$, indicating prolate deformation, and takes nearly vanishing values, $\chi_\nu + \chi_\pi \approx 0$, around the neutron midshell $N = 66$, reflecting γ softness. However, for $N \geqslant 70$, the sum is negative (positive) in the mapped (phenomenological) calculations, implying prolate (oblate) deformation. Note that a fixed value $\chi_\pi = 0.2$ is employed in the phenomenological IBM-2 calculations, whereas in the mapped approach this parameter exhibits a strong nucleon number dependence.

The $B(E2)$ transition probabilities, computed within the mapped and phenomenological IBM-2 models, are plotted in Fig. 5 as functions of the neutron number N. The same $E2$ effective boson charge is used for the quadrupole operators in the two sets of the IBM-2 calculations. The $B(E2; 2_1^+ \to 0_1^+)$ and $B(E2; 4_1^+ \to 2_1^+)$ values obtained in the mapped IBM-2 calculations agree reasonably well with the experiment, exception made of ^{112}Pd. Both the mapped and phenomenological IBM-2 calculations predict $B(E2; 0_2^+ \to 2_1^+)$ and $B(E2; 2_2^+ \to 2_1^+)$ rates with similar trends as functions of N. However, the mapped IBM-2 scheme provides smaller $B(E2; 0_2^+ \to 2_1^+)$ values for Pd isotopes with $58 \leqslant N \leqslant 62$. The enhancement of the predicted $B(E2; 2_2^+ \to 2_1^+)$ transition rates around the midshell $N = 66$ [see Fig. 5(d)] can be considered as another signature of γ-soft deformation.

IV. ODD-*A* Pd and Rh NUCLEI

The excitation energies of the low-lying positive-parity states obtained for the odd-A Pd isotopes ${}^{105-123}$Pd are depicted in Fig. 6. The results obtained within the IBFM-2 model with boson-core Hamiltonian determined by mapping the Gogny-D1M EDF [Fig. 6(a)] and those obtained from phenomenological calculations of Ref. [37] [Fig. 6(b)] are compared with experimental data [70–72]. The two IBFM-2 calculations, using different boson-core Hamiltonian parameters, provide an overall consistent description of the experimental excitation energies. As can be seen from the

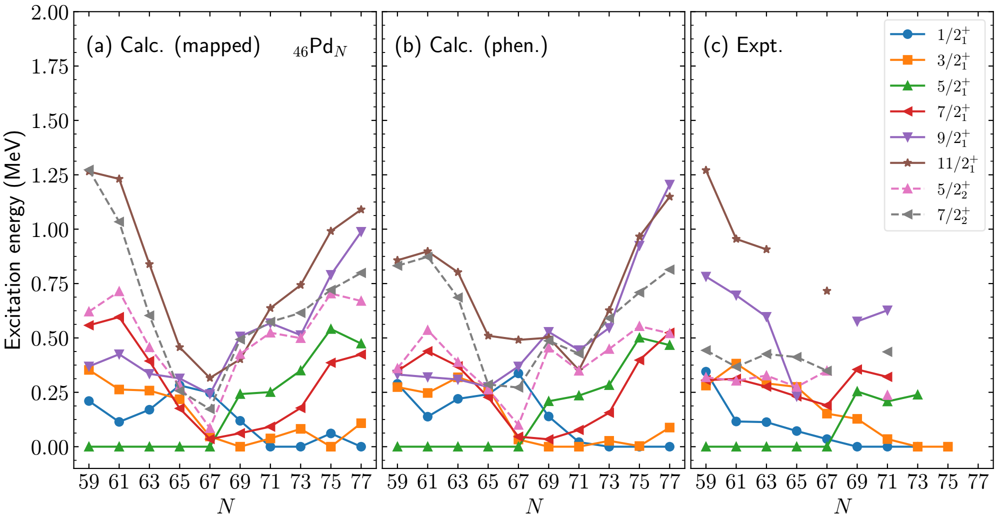

FIG. 6. Excitation energies of the low-lying positive-parity states obtained for odd-A Pd isotopes within the IBFM-2 with the boson-core Hamiltonian determined by (a) mapping the Gogny-D1M EDF and (b) using the phenomenological fit. The experimental data included in panel (c) are taken from Ref. [71] for ^{117}Pd, from Ref. [72] for ^{119}Pd, and from the NNDC database [70] for the other nuclei.

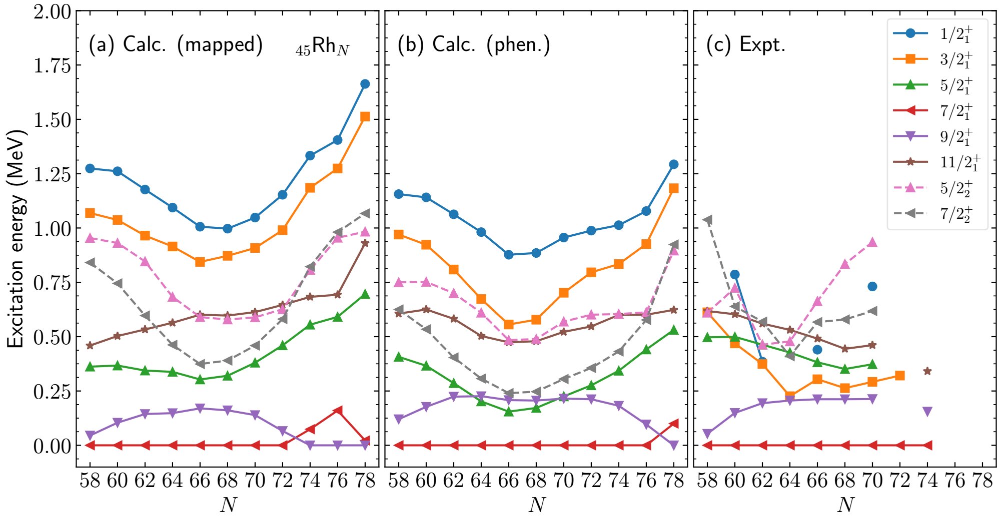

FIG. 7. The same as Fig. 6, but for odd-Z Rh nuclei. The experimental data are taken from Ref. [70].

figure, the experimental data display a change in the ground-state spin from $N = 67$ to 69. The corresponding even-even core nuclei, ^{114}Pd and ^{116}Pd, are in the transitional region, for which the potential-energy surfaces are suggested to be considerably γ soft (see Fig. 2). The sudden change in the ground-state spin of the odd-A neighbor, therefore, reflects the transition that takes place in the even-even core systems from the γ unstable shape, which is associated with an O(6)-like potential, to the E(5)-like structure characterized by a flat-bottomed potential.

The excitation energies of the low-lying positive-parity states obtained for the odd-A isotopes $^{103\text{–}123}$Rh are depicted in Fig. 7. Experimentally, the ground states of these isotopes have spin $I^{\pi} = 7/2^{+}$. Exceptions are made of some of the heaviest isotopes, and similar results are predicted within both the mapped and phenomenological calculations. Both theoretically and experimentally, some of the energy levels exhibit an approximate parabolic behavior with a minimum around the middle of the major shell, $N \approx 66$. For $^{103\text{–}123}$Rh, the order of most of the energy levels remains unchanged in the whole isotopic chain within both the mapped and phenomenological IBFM-2 calculations. This situation is in a sharp contrast with the one in the odd-A Pd (see Fig. 6), in which the structural change along the isotopic chain occurs more rapidly. Note that the low-lying states of the odd-A Rh nuclei are accounted for almost purely by the proton $\pi 0g_{9/2}$ single-particle configuration while more than one single-particle orbital is considered for the odd-A Pd. The occupation number of the odd proton in the $\pi 0g_{9/2}$ orbital is also nearly constant along the whole Rh isotopic chain [see Fig. 1(f)], whereas the occupation probabilities for the odd neutron in the odd-A Pd vary significantly with N [see Fig. 1(e)]. Furthermore, as shown below, the strength parameters for $\hat{V}_{\mathrm{BF}}$ are fixed in the case of odd-A Rh nuclei while they depend on the boson number for odd-A Pd isotopes.

The strength parameters of the boson-fermion interaction (4) for odd-N Pd nuclei are shown in Fig. 8. These parameters are chosen so that the ground-state spin and energies of a few low-lying levels are reproduced reasonably well. The parameters for the two IBFM-2 calculations are rather similar, with an exception made of the monopole strength A_{ν} for $59 \leqslant N \leqslant 63$. Note that common quasiparticle energies $\tilde{\epsilon}_{j_\rho}$ and occupation probabilities $v_{j_\rho}^2$ are used for both IBFM-2 calculations. The parameters for the ^{123}Pd$_{77}$ nucleus, where no experimental data are available, are taken to be the same as those for the adjacent nucleus ^{121}Pd$_{75}$. As can be seen from the figure, the IBFM-2 parameters turn out to have a strong N dependence that reflects the rapid structural change in the odd-A Pd isotopes. On the other hand, constant strength parameters $\Gamma_{\pi} = 0.6$ (0.0) MeV, $\Lambda_{\pi} = 0.6$ (0.75) MeV, and $A_{\pi} = 0.0$ (-0.25) MeV reproduce reasonably well the experimental data for odd-A Rh nuclei in the mapped (phenomenological) calculations.

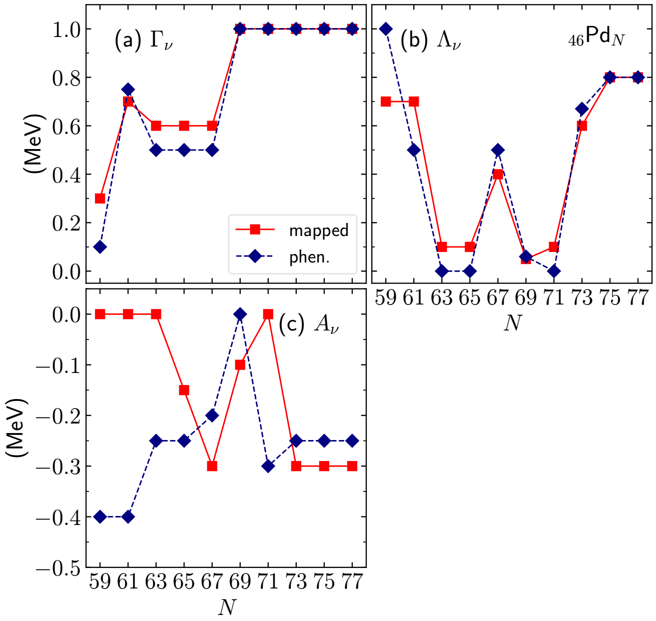

FIG. 8. Parameters of the mapped and phenomenological IBFM-2 Hamiltonian (2) for odd-N Pd nuclei.

TABLE II. $B(E2)$ rates (in Weisskopf units, W.u.), quadrupole moment $Q(I)$ (in e b), $B(M1)$ rates (in W.u. × 10^{-3}), and magnetic-dipole moments $\mu(I)$ (in μ_N) obtained for odd-A Pd nuclei within the mapped and phenomenological IBFM-2 calculations. Experimental data are taken from Refs. [70,73].

		Calc.		
		Mapped	Phen.	Expt.
^{105}Pd	$B(E2;1/2^+_1 \to 3/2^+_1)$	25	13	2.0^{+91}_{-16}
	$B(E2;1/2^+_1 \to 5/2^+_1)$	90	45	2.64(15)
	$B(E2;1/2^+_2 \to 3/2^+_1)$	0.6	3.1	0.9^{+12}_{-7}
	$B(E2;1/2^+_2 \to 5/2^+_1)$	0.04	0.9	8.4(9)
	$B(E2;3/2^+_1 \to 5/2^+_1)$	44	40	4.6(7)
	$B(E2;3/2^+_1 \to 3/2^+_3)$	0.05	5.1	>0.21
	$B(E2;3/2^+_3 \to 5/2^+_2)$	0.01	2.7	>2.2
	$B(E2;5/2^+_1 \to 5/2^+_2)$	15	29	1.8(4)
	$B(E2;7/2^+_1 \to 5/2^+_1)$	24	33	0.30(4)
	$B(E2;9/2^+_1 \to 5/2^+_1)$	57	40	14.3(13)
	$B(M1;1/2^+_1 \to 3/2^+_1)$	372	280	14.9^{+20}_{-21}
	$B(M1;1/2^+_1 \to 1/2^+_2)$	0.93	1.5	7.8(8)
	$B(M1;1/2^+_2 \to 3/2^+_1)$	37	7	45^{+6}_{-5}
	$B(M1;3/2^+_1 \to 5/2^+_1)$	31	4.4	20.3(22)
	$B(M1;3/2^+_1 \to 3/2^+_3)$	0.012	0.0004	>5.9
	$B(M1;3/2^+_3 \to 5/2^+_2)$	0.0026	2.9	>47
	$B(M1;5/2^+_1 \to 5/2^+_2)$	13	1.6	19(3)
	$B(M1;5/2^+_3 \to 3/2^+_1)$	4.7	0.47	>0.40
	$B(M1;5/2^+_3 \to 7/2^+_2)$	52	32	>25
	$B(M1;7/2^+_1 \to 5/2^+_1)$	31	3.7	10.6(12)
	$Q(5/2^+_1)$	−0.54	−0.27	+0.660(11)
	$\mu(3/2^+_1)$	−0.56	−0.64	−0.074(13)
	$\mu(5/2^+_1)$	−1.19	−1.32	−0.642(3)
	$\mu(5/2^+_2)$	−0.67	−0.76	+0.95(20)
^{107}Pd	$B(E2;1/2^+_1 \to 5/2^+_1)$	112	90	0.58(7)
	$\mu(5/2^+_1)$	−1.06	−1.05	0.735(7)
^{109}Pd	$B(E2;1/2^+_1 \to 5/2^+_1)$	97	76	1.36(18)
	$B(E2;3/2^+_1 \to 5/2^+_1)$	58	48	8(8)
	$B(M1;3/2^+_1 \to 5/2^+_1)$	4.4	4.4	2.2(8)
	$B(M1;5/2^+_2 \to 3/2^+_1)$	159	142	11.7(19)
	$B(M1;7/2^+_2 \to 5/2^+_1)$	3.2	0.13	3.6(4)

Experimental data for electromagnetic transitions and moments are available for odd-A Pd and Rh nuclei with $N \leqslant 65$. The predicted $B(E2)$ and $B(M1)$ transition strengths as well as the electric-quadrupole $Q(I^\pi)$ and magnetic-dipole $\mu(I^\pi)$ moments for the low-lying positive-parity states in odd-A Pd are given in Table II. In most of the cases, the mapped and phenomenological calculations provide similar results. Large values are obtained for the $B(E2;1/2^+_1 \to 5/2^+_1)$ (in ^{105}Pd, ^{107}Pd, and ^{109}Pd), $B(E2;3/2^+_1 \to 5/2^+_1)$ (in ^{105}Pd and ^{109}Pd), and $B(E2;9/2^+_1 \to 5/2^+_1)$ (in ^{105}Pd) transitions. The experimental data, however, suggest that these $E2$ transitions are weaker. The $B(E2)$ and $B(M1)$ rates corresponding to some transitions in odd-A Rh nuclei are given in Table III. The large $B(E2;5/2^+_1 \to 7/2^+_1)$ and $B(E2;5/2^+_1 \to 9/2^+_1)$ rates obtained for ^{103}Rh overestimate the experimental rates by several orders of magnitude.

TABLE III. The same as in Table II, but for odd-A Rh nuclei.

		Calc.		
		Mapped	Phen.	Expt.
^{103}Rh	$B(E2;5/2^+_1 \to 7/2^+_1)$	33	31	2.0(6)
	$B(E2;5/2^+_1 \to 9/2^+_1)$	28	13	0.107(33)
	$B(M1;5/2^+_1 \to 7/2^+_1)$	471	354	40(12)
	$B(M1;9/2^+_1 \to 7/2^+_1)$	1.0	1.9	43(12)
	$\mu(7/2^+_1)$	4.85	4.88	+4.540(11)
	$\mu(9/2^+_1)$	5.69	5.62	+4.9(8)
^{107}Rh	$B(E2;3/2^+_1 \to 7/2^+_1)$	4.73	1.62	0.16(2)
^{109}Rh	$B(E2;3/2^+_1 \to 3/2^+_2)$	0.14	0.18	$1.7 \times 10^2(5)$
	$B(E2;3/2^+_1 \to 7/2^+_1)$	4.41	0.01	0.0174(5)
	$B(E2;3/2^+_2 \to 7/2^+_1)$	5.3	5.9	26.1(19)
	$B(E2;5/2^+_1 \to 9/2^+_1)$	7.9	5.3	>23
	$B(E2;5/2^+_2 \to 3/2^+_1)$	12	5.8	1.7(7)
	$B(E2;5/2^+_2 \to 3/2^+_2)$	22	9	$7.E+1(3)$
	$B(E2;7/2^+_2 \to 3/2^+_1)$	8	15	131(12)
	$B(M1;5/2^+_1 \to 3/2^+_3)$	5.2	8.6	>220
	$B(M1;5/2^+_1 \to 3/2^+_1)$	818	414	>0.40
	$B(M1;5/2^+_2 \to 3/2^+_1)$	37	289	2.4(3)
	$B(M1;5/2^+_2 \to 3/2^+_2)$	152	207	2.2(15)
	$B(M1;5/2^+_2 \to 3/2^+_3)$	18	210	2.5(4)
	$B(M1;5/2^+_2 \to 7/2^+_1)$	231	112	$4.1\times10^{-2}(6)$
	$B(M1;7/2^+_2 \to 9/2^+_1)$	318	611	0.25(6)
	$B(M1;7/2^+_1 \to 7/2^+_2)$	7.6	8.9	$6.6\times10^{-2}(8)$
	$B(M1;3/2^+_1 \to 3/2^+_2)$	27	48	0.58(12)
	$B(M1;3/2^+_1 \to 3/2^+_3)$	158	256	1.18(11)
	$B(M1;3/2^+_2 \to 3/2^+_3)$	276	32	0.32(10)
	$B(M1;5/2^+_1 \to 7/2^+_1)$	233	172	>3.2
	$B(M1;9/2^+_1 \to 7/2^+_1)$	4.3	18	>58

The deviation of the predicted $B(E2)$ and $B(M1)$ transition rates for odd-A systems with respect to the experiment could be interpreted in terms of the structure of the corresponding IBFM-2 wave functions. The components of the IBFM-2 wave functions for the low-lying states of odd-A Pd isotopes are shown in Fig. 9. They are associated with the single(quasi)-particle orbitals $\nu 2s_{1/2}$, $\nu 1d_{3/2}$, $\nu 1d_{5/2}$, and $\nu 0g_{7/2}$. Only components obtained within the mapped framework are shown as illustrative examples, while qualitatively similar results are obtained using the phenomenological approach. The states considered for odd-A Rh nuclei are almost purely made of the proton $0g_{9/2}$ configuration (with a weight of ≈99%). Therefore, the corresponding wave-function contents are not shown in the plot. As can be seen from the figure, the neutron $1d_{5/2}$ configuration accounts for most of the IBFM-2 wave functions for the $1/2^+_1$, $3/2^+_1$, $5/2^+_1$, and $7/2^+_1$ in odd-A Pd nuclei with $N \lesssim 67$. However, the description of these wave functions in both the mapped and phenomenological IBFM-2 calculations in the present study may not be adequate, and this leads to some of the considerable disagreements between the calculated and experimental electromagnetic properties, including the $B(E2;1/2^+_1 \to 5/2^+_1)$ values in ^{105}Pd, ^{107}Pd, and ^{109}Pd (see Table II). The deficiency of the IBFM-2 wave functions could arise from various deficiencies of the present model calculations, such as the choice of the single-particle space, the quasiparticle energies and occupation probabilities of the odd particle, and the effective charges involved in the transition operators, which are kept

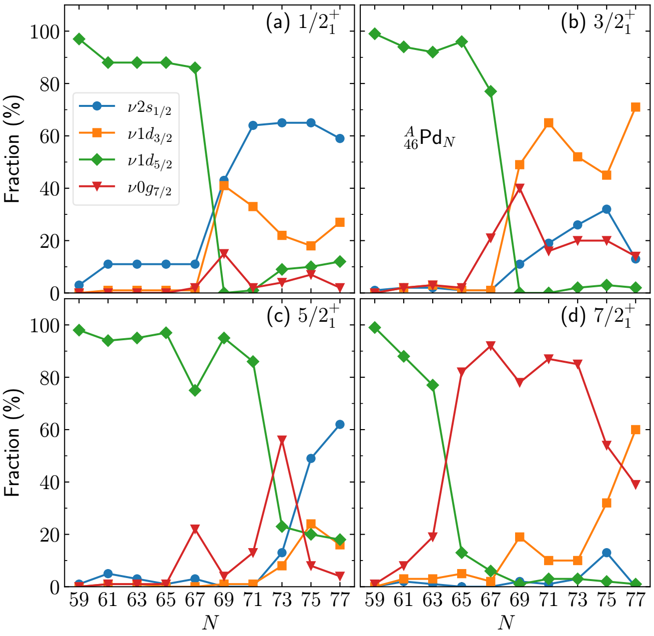

FIG. 9. Fractions (in percent) of the neutron $\nu 2s_{1/2}$, $\nu 1d_{3/2}$, $\nu 1d_{5/2}$, and $\nu 0g_{7/2}$ single-particle configurations in the wave functions for the (a) $1/2_1^+$, (b) $3/2_1^+$, (c) $5/2_1^+$, and (d) $7/2_1^+$ states in odd-*A* Pd nuclei. The wave functions are obtained within the mapped IBFM-2 scheme based on Gogny-D1M EDF calculations.

constant for all nuclei. On the other hand, earlier IBFM-2 fitting calculations in the same mass region [7,74] obtained $E2$ and $M1$ properties consistent with experiment.

V. ODD-ODD Rh NUCLEI

The excitation energies of the low-lying positive-parity states obtained for odd-odd Rh isotopes are depicted in Fig. 10. The available experimental data [70] suggest that for $N \leqslant 71$ the ground state has spin $I^\pi = 1^+$. Excited 1^+ states are also observed at low energy. Both the mapped [Fig. 10(a)] and phenomenological [Fig. 10(b)] IBFFM-2 calculations account for the ground-state spin 1^+. The calculations also reproduce reasonably well the energies of the 1_2^+ states. From $N \approx 71$ to 73, both types of calculations suggest a change in the ground-state spin to $I^\pi = 5^+$. There are no spectroscopic data to compare with for even-*A* Rh isotopes with $N \geqslant 73$. Note, that a ground-state spin different from $I^\pi = 1^+$ is experimentally found in the neighboring odd-odd Ag and In isotopes. For instance, for ^{120}Ag, ^{122}Ag, ^{124}Ag, and ^{126}In the ground state has spin $I^\pi = 3^+$. A low-lying 5^+ level is observed in ^{122}In at an excitation energy around 40 keV above the 1^+ ground state.

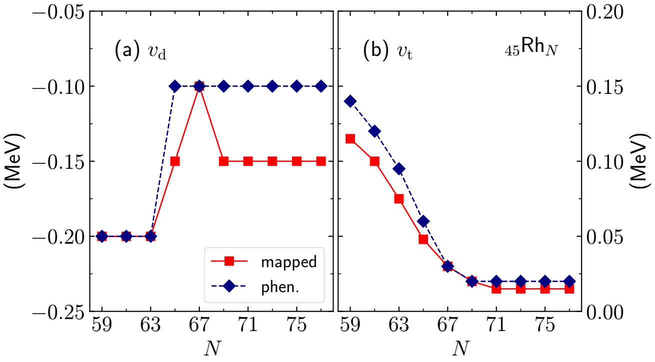

FIG. 11. Parameters for the residual neutron-proton interactions (8) employed for odd-odd Rh isotopes in the mapped and phenomenological IBM approaches.

The strength parameters v_d and v_t of the neutron-proton residual interaction $\hat{V}_{\nu\pi}$ in Eq. (8) are shown in Fig. 11 for odd-odd Rh isotopes as functions of the neutron number. Those parameters are determined so that the correct ground-state spin $I^\pi_{g.s.} = 1_1^+$ as well as the energy of the 1_2^+ state are reproduced reasonably well. For $N \geqslant 73$, where experimental data are not available, the same values of the parameters as for ^{116}Rh$_{71}$ are employed. As can be seen from Fig. 11(a), the parameter v_d changes suddenly from $N = 63$ to 67. This

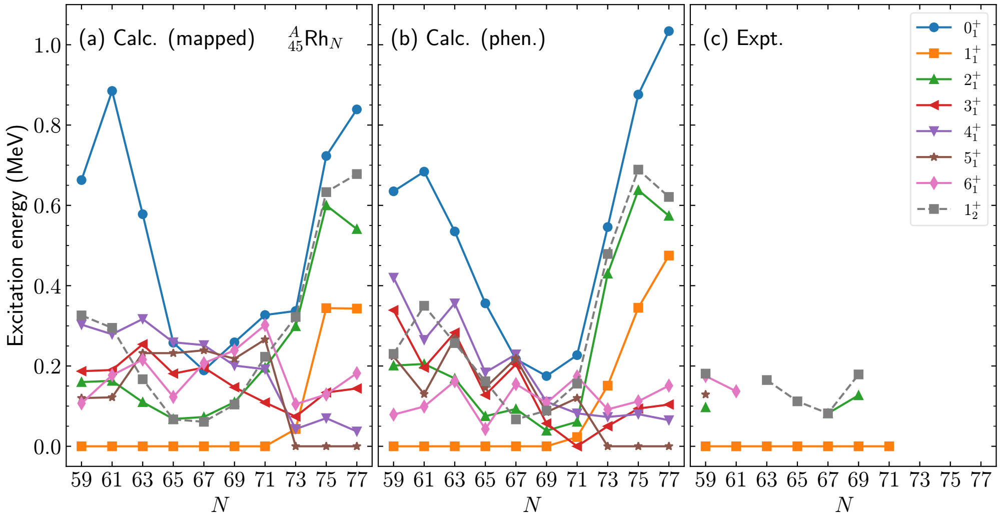

FIG. 10. The same as Fig. 6, but for the odd-odd Rh isotopes.

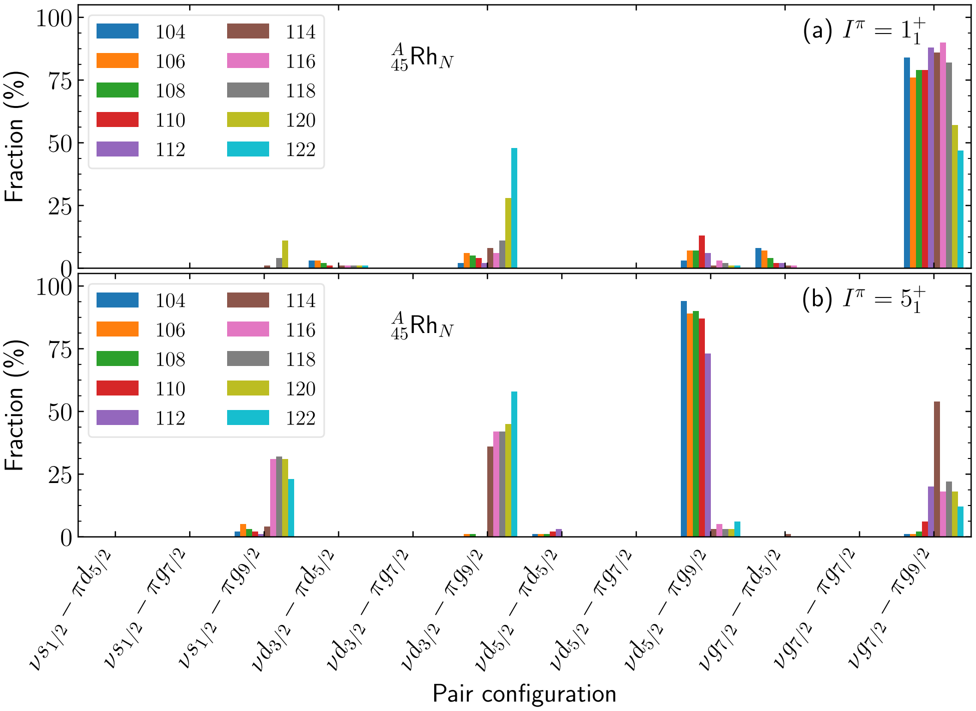

FIG. 12. Fraction (in percent) of the neutron-proton pair components in the wave functions for the (a) 1_1^+ and (b) 5_1^+ states of the odd-odd $^{104-122}$Rh isotopes under study. The wave functions are obtained within the mapped IBFFM-2 formalism based on the Gogny-D1M EDF.

sudden change accounts for the experimental [see Fig. 10(c)] lowering of the 1_2^+ level toward the middle of the major shell, $N \approx 67$. On the other hand, the tensor interaction strength exhibits a smooth decrease with N.

The nature of the low-lying states in odd-odd Rh isotopes can be analyzed in terms of various neutron-proton pair components in the IBFFM-2 wave functions. The corresponding results for the 1_1^+ and 5_1^+ states, obtained within the mapped IBFFM-2 formalism, are shown in Fig. 12. For nuclei with $A \leqslant 118$, the 1_1^+ state is mostly based on the configuration associated with the $[\nu 0g_{7/2} \otimes \pi 0g_{9/2}]^{(J)}$ neutron-proton pairs coupled to the even-even boson core, with the total angular momentum of the fermion system $J = 1, 2, \ldots, 8$. For ^{120}Rh and ^{122}Rh, the contributions of the $[\nu 1d_{3/2} \otimes \pi 0g_{9/2}]^{(J)}$ ($J = 3, 4, 5, 6$) pairs also play a prominent role. As one can see from Fig. 12(b), the dominant contribution to the 5_1^+ wave function for Rh isotopes with mass $A \leqslant 112$ comes from the $[\nu 1d_{5/2} \otimes \pi 0g_{9/2}]^{(J)}$ pair components, while the $[\nu 0g_{7/2} \otimes \pi 0g_{9/2}]^{(J)}$ pair components play a negligible role. For heavier Rh isotopes, with $A \geqslant 114$, the other pair components that involve the $\pi 0g_{9/2}$ state, i.e., those based on the $[\nu 2s_{1/2} \otimes \pi 0g_{9/2}]^{(J)}$, $[\nu 1d_{3/2} \otimes \pi 0g_{9/2}]^{(J)}$, and $[\nu 0g_{7/2} \otimes \pi 0g_{9/2}]^{(J)}$ pairs, are rather fragmented in the $I^{\pi} = 5_1^+$ wave functions. Qualitatively similar results are obtained using phenomenological IBFFM-2 wave functions.

The experimental information on the electromagnetic properties of the considered odd-odd Rh nuclei is rather limited. Table IV compares the predicted and experimental $B(E2)$, $B(M1)$, and magnetic-dipole moment $\mu(1_1^+)$ for ^{104}Rh and ^{106}Rh. Both the mapped and phenomenological IBFFM-2 calculations provide a reasonable description of the experimental data for these odd-odd nuclei. Nevertheless, a more detailed assessment of the quality of the IBFFM-2 wave functions is difficult in this case due to the lack of data.

VI. β DECAY

A. β decays between odd-A nuclei

Figure 13 shows the $\log ft$ values for the β^- decays of the $7/2_1^+$ state of the odd-A Rh into several low-lying states of the odd-A Pd nuclei. Results are obtained using mapped and phenomenological IBFM-2 wave functions. In both cases, the predicted trend of the $\log ft$ values, as functions of the nucleon number, reflects the structural change in the parent and daughter odd-A nuclei. An illustrative example is a kink emerging at the mass $A \approx 113$ or 115 in the predicted $\log ft$ values for the $7/2_1^+ \rightarrow 5/2_1^+$ [Fig. 13(a)] and $7/2_1^+ \rightarrow 7/2_1^+$

TABLE IV. $B(E2)$, $B(M1)$ (in W.u.), and magnetic-dipole moment $\mu(1_1^+)$ (in μ_N) for odd-odd Rh isotopes, computed within the mapped IBFFM-2 based on the Gogny-D1M EDF and the phenomenological IBFFM-2. Experimental data are taken from Refs. [70,73].

		Calc.		
		Mapped	Phen.	Expt.
^{104}Rh	$B(E2; 1_3^+ \rightarrow 2_1^+)$	1.35	13	>5.2
	$B(M1; 2_1^+ \rightarrow 1_1^+)$	0.03	0.06	>0.029
	$B(M1; 1_3^+ \rightarrow 1_1^+)$	0.03	0.05	>0.00098
^{106}Rh	$\mu(1_1^+)$	2.13	2.20	2.575(7)

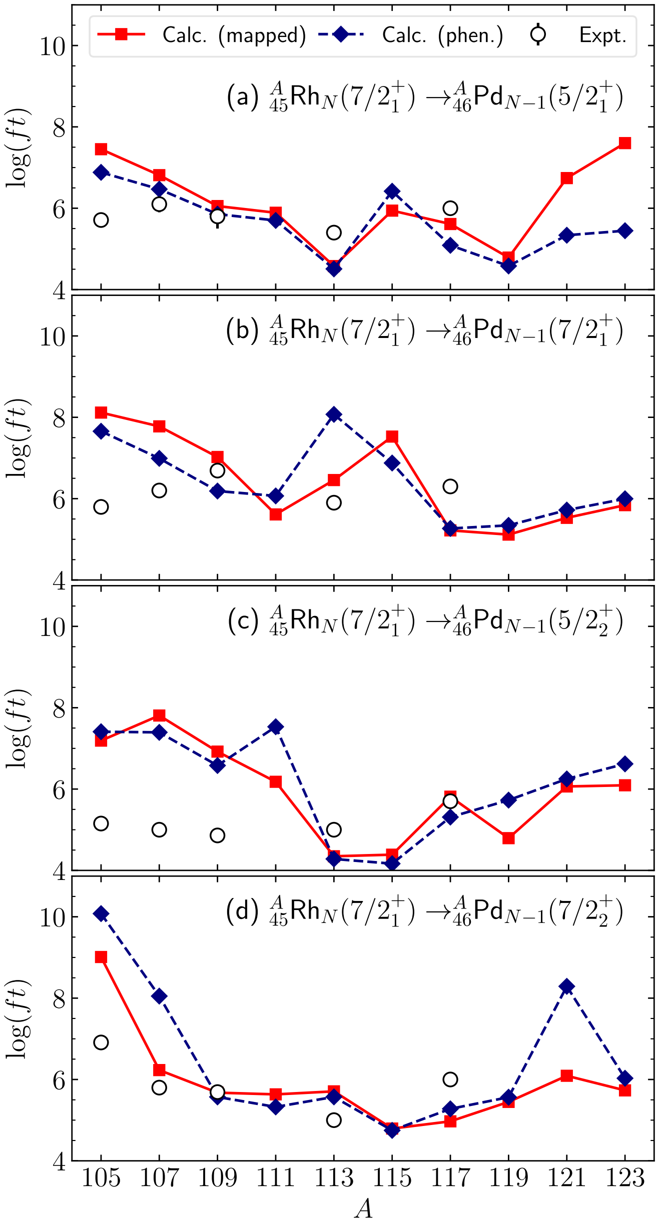

FIG. 13. log *ft* values for the β^- decays from the odd-*A* Rh into Pd nuclei, (a) $7/2^+_1 \to 5/2^+_1$, (b) $7/2^+_1 \to 7/2^+_1$, (c) $7/2^+_1 \to 5/2^+_2$, and (d) $7/2^+_1 \to 7/2^+_2$ computed using wave functions obtained within the mapped and phenomenological IBFM-2 models. The available experimental data [70] are also included in the plot.

[Fig. 13(b)] decays. The mass number at which the kink emerges corresponds to the transitional region, where the ground-state spin changes, observed in the odd-*A* Pd daughter (see Fig. 6). The mass dependence of the predicted log *ft* values is similar in the mapped and phenomenological calculations, exception made of the results from $A = 113$ to 115 in the $7/2^+_1 \to 7/2^+_1$ decay and from $A = 117$ to 119 in the $7/2^+_1 \to 5/2^+_2$ decay.

Both within the mapped and phenomenological schemes, the present calculations overestimate the observed log *ft* values for the decays $^{105,107}\mathrm{Rh}(7/2^+_1) \to {}^{105,107}\mathrm{Pd}(5/2^+_1)$ [Fig. 13(a)]. At both $A = 105$ and 107, the $5/2^+_1$ final-state wave function has been shown to be almost purely made of the $\nu 1d_{5/2}$ configuration [see Fig. 9(c)], while the parent state $7/2^+_1$ is of almost pure $\pi 0g_{9/2}$ nature.

The dominant contribution to the GT matrix element for the above $7/2^+_1 \to 5/2^+_1$ decays indeed comes from the term that corresponds to the coupling of the $\nu 1d_{5/2}$ with $\pi 0g_{9/2}$ single-particle states, which is of the form

$$[[\tilde{d}_\nu \times a^\dagger_{\nu 1d_{5/2}}]^{(7/2)} \times \tilde{a}_{\pi 0g_{9/2}}]^{(J=1)}. \tag{23}$$

The matrix element of this term is, however, rather small: 0.041 and −0.091 (0.069 and −0.118), for the ^{105}Rh and ^{107}Rh decays in the mapped (phenomenological) approach. There are many other terms similar to the one in Eq. (23), but their matrix elements are small and cancel each other, leading to a small GT transition rate. The same is true for the $^{105,107}\mathrm{Rh}(7/2^+_1) \to {}^{105,107}\mathrm{Pd}(7/2^+_1)$ decays [Fig. 13(b)]. In this case, the Fermi transition matrix is also negligibly small.

The calculations underestimate the log *ft* values for the $^{113}\mathrm{Rh}(7/2^+_1) \to {}^{113}\mathrm{Pd}(5/2^+_1)$ decay. For this decay, approximately 75% and 25% of the wave function of the $5/2^+_1$ final state are comprised of the $\nu 1d_{5/2}$ and $\nu 0g_{7/2}$ configurations, respectively [see Fig. 9(c)]. Due to the large admixture of the $\nu 0g_{7/2}$ components into the $5/2^+_1$ state of ^{113}Pd, the term that is proportional to

$$[a^\dagger_{0\nu g_{7/2}} \times \tilde{a}_{\pi 0g_{9/2}}]^{(1)} \tag{24}$$

makes a sizable contribution to the GT transition strength. The matrix element of this component, which amounts to −0.788 (0.850) in the mapped (phenomenological) calculation, is so large that the corresponding log *ft* value is too small as compared with the experimental value.

As noted above, there are notable quantitative differences between the mapped and phenomenological predictions for the log *ft* values in the case of the $^{113}\mathrm{Rh}(7/2^+_1) \to {}^{113}\mathrm{Pd}(7/2^+_1)$ decay. The GT transition matrix element obtained in the phenomenological calculation is two orders of magnitude smaller than the one obtained within the mapped scheme. This difference stems from a subtle balance between matrix elements of different terms in the GT transition operator. The dominant contribution to the GT matrix element in the former calculation come from the term proportional to the expression in Eq. (24), and the one of the form

$$s^\dagger_\nu[[\tilde{d}_\nu \times a^\dagger_{\nu 0g_{7/2}}]^{(7/2)} \times a_{\pi 0g_{9/2}}]^{(1)}. \tag{25}$$

Their matrix elements are of the same order of magnitude but have the opposite signs, hence cancellation occurs between these terms. The degree of the cancellation, however, is much smaller in the mapped calculation. The contribution of the Fermi matrix element is negligibly small in both the mapped and phenomenological cases.

The log *ft* values for the Rh decays into the non-yrast states, $5/2^+_2$ and $7/2^+_2$, of the odd-*A* Pd are shown in Figs. 13(c) and 13(d), respectively. The predicted log *ft* values for the $^{A}\mathrm{Rh}(7/2^+_1) \to {}^{A}\mathrm{Pd}(5/2^+_2)$ decay in the two sets of calculations are generally large, log $ft \gtrsim 7$ for $A \lesssim 111$. In particular, they overestimate the experimental values for

TABLE V. $\log ft$ values for the β^- decays from odd-A Rh into Pd nuclei, computed using wave functions obtained within the mapped IBFM-2 scheme based on the Gogny-D1M EDF and within the phenomenological IBFM-2 model. The experimental data are taken from Ref. [70].

		Calc.		
Decay	$I_i \to I_f$	Mapped	Phen.	Expt.
^{105}Rh → ^{105}Pd	$7/2_1^+ \to 5/2_1^+$	7.45	6.88	5.710(7)
	$7/2_1^+ \to 7/2_1^+$	8.12	7.66	5.797(16)
	$7/2_1^+ \to 5/2_2^+$	7.19	7.41	5.152(20)
	$7/2_1^+ \to 7/2_2^+$	9.01	10.08	6.91(3)
^{107}Rh → ^{107}Pd	$7/2_1^+ \to 5/2_1^+$	6.81	6.47	6.1(2)
	$7/2_1^+ \to 5/2_2^+$	7.81	7.39	5.0(1)
	$7/2_1^+ \to 7/2_1^+$	7.78	6.99	6.2(1)
	$7/2_1^+ \to 7/2_2^+$	6.23	8.05	5.8(1)
	$7/2_1^+ \to 5/2_3^+$	8.00	7.45	6.1(1)
	$7/2_1^+ \to 5/2_4^+$	5.82	7.87	5.3(1)
^{109}Rh → ^{109}Pd	$7/2_1^+ \to 5/2_1^+$	6.05	5.86	5.8(3)
	$7/2_1^+ \to 7/2_1^+$	7.02	6.19	6.69(12)
	$7/2_1^+ \to 5/2_2^+$	6.92	6.58	4.86(5)
	$7/2_1^+ \to 7/2_2^+$	5.68	5.57	5.69(6)
	$7/2_1^+ \to 5/2_3^+$	6.83	7.39	5.53(5)
	$7/2_1^+ \to 9/2_1^+$	7.32	6.84	7.26(19)
^{113}Rh → ^{113}Pd	$7/2_1^+ \to 5/2_1^+$	4.58	4.51	5.4(1)
	$7/2_1^+ \to 7/2_1^+$	6.46	8.07	5.90(5)
	$7/2_1^+ \to 5/2_2^+$	4.35	4.28	5.00(4)[a]
	$7/2_1^+ \to 7/2_2^+$	5.71	5.57	5.00(4)[a]
	$7/2_1^+ \to 5/2_3^+$	5.42	5.59	6.7(2)[b]
	$7/2_1^+ \to 7/2_3^+$	5.07	4.81	6.7(2)[b]
^{117}Rh → ^{117}Pd	$7/2_1^+ \to 5/2_1^+$	5.61	5.09	6.0[c]
	$7/2_1^+ \to 5/2_2^+$	5.81	5.31	5.7[c]
	$7/2_1^+ \to 5/2_3^+$	4.27	5.34	5.8[c]
	$7/2_1^+ \to 7/2_1^+$	5.22	5.27	6.3[c]
	$7/2_1^+ \to 5/2_4^+$	7.64	4.56	6.3[c]
	$7/2_1^+ \to 5/2_5^+$	5.82	5.50	6.0[d]
	$7/2_1^+ \to 7/2_2^+$	4.97	5.28	6.0[d]

[a] $(5/2^+, 7/2^+)$ at 349 keV [70].

[b] $(5/2^+, 7/2^+)$ at 373 keV based on the XUNDL datasets [70].

[c] Uncertainties are not given with the $\log ft$.

[d] $(5/2^+, 7/2^+)$ level at 436 keV, based on the XUNDL datasets [70]. Uncertainties are not given.

the ^{105}Rh, ^{107}Rh, and ^{109}Rh decays by a factor of two. The discrepancy could be attributed to the nature of the IBFM-2 wave functions and the components of the GT operator. The computed $\log ft$ values for the ^{A}Rh$(7/2_1^+) \to {}^A$Pd$(7/2_2^+)$ decay in the mapped scheme are close to the experimental values, with an exception made of the ^{105}Rh decay.

Table V gives complementary results for the $\log ft$ values of the β^- decays ^{A}Rh$(7/2_1^+) \to {}^A$Pd(I_f^+), with final states other than those already discussed above. The predicted $\log ft$ values are compared with the available experimental data [70].

Previous IBFM-2 calculations [7] provided $\log ft$ values for the β^- decays $7/2_1^+ \to 5/2_1^+$ and $7/2_1^+ \to 7/2_1^+$ in ^{105,107,109}Rh which are consistent with the experimental ones. However, for the same nuclei the values $\log ft \approx 4$ were obtained for the $7/2_1^+ \to 5/2_2^+$ β^- decay. Such $\log ft$ values are systematically smaller than the experimental values and those obtained in this work. A more recent IBFM-2 calculation for the ^{115,117}Rh $\to$ ^{115,117}Pd β^- decay [13] obtained a value $\log ft = 5.90$ for the $7/2_1^+ \to 5/2_1^+$ decay of ^{115}Rh. This $\log ft$ value is close to the one obtained in this study. On the other hand, for the $7/2_1^+ \to 5/2_1^+$ and $7/2_1^+ \to 7/2_1^+$ decays of ^{117}Rh, the values $\log ft = 6.78$ and 6.68 were reported in Ref. [13]. They are approximately 20% larger than those obtained in the present work.

B. β decays of even-A nuclei

The $\log ft$ values for the β^- decays of the even-A Rh into Pd nuclei are plotted in Fig. 14. One immediately sees from Fig. 14(a) that the mapped and phenomenological $\log ft$ values for the ^{A}Rh$(1_1^+) \to {}^A$Pd(0_1^+) decays are, approximately, a factor two smaller than the experimental ones. The corresponding GT matrix elements are almost purely determined by the contributions of the terms associated with the $\nu 0g_{7/2} - \pi 0g_{9/2}$ coupling, i.e.,

$$[\tilde{a}_{\nu 0g_{7/2}} \times \tilde{a}_{\pi 0g_{9/2}}]^{(1)}, \tag{26}$$

for $N \leqslant 65$ and

$$s_\nu^\dagger[\tilde{a}_{\nu 0g_{7/2}} \times \tilde{a}_{\pi 0g_{9/2}}]^{(1)}, \tag{27}$$

for $N \geqslant 67$. As shown in Fig. 15(a), the matrix elements of these terms are particularly large for the mass $A \leqslant 116$. Note also that the IBFFM-2 wave functions for the initial 1_1^+ state mainly consist of the pair configuration $[\nu 0g_{7/2} \otimes \pi 0g_{9/2}]^{(J)}$ for the even-A Rh with $A \leqslant 118$ [see Fig. 12(a)]. For the larger mass $A \geqslant 120$, this pair configuration becomes less important in the 1_1^+ wave function of the final nucleus. As a consequence, the GT transition strength decreases with increasing A [see Fig. 15(a)].

To reproduce the β-decay $\log ft$ data, effective values of the $g_{\rm A}$ factor, $g_{\rm A,eff}$, are often employed. Here we compare the predicted $\log ft$ value for the ^{A}Rh$(1_1^+) \to {}^A$Pd(0_1^+) decay with the corresponding experimental one, and extract the $g_{\rm A,eff}$ values for those decays for which $\log ft$ data are available. The resulting $g_{\rm A,eff}$ values are, on average, $g_{\rm A,eff} \approx 0.152$ (0.205) in the mapped (phenomenological) scheme. This amounts to a reduction of the free value by approximately by 88 (84)%. In the previous IBM-2/IBFFM-2 study of the β and $\beta\beta$ decays of the Te and Xe isotopes with $A \approx 130$ [9], the $g_{\rm A,eff}$ values extracted from a comparison with the $\log ft$ data for the single-β decays are 0.313 for the β^+ decay ^{128}I$(1_1^+) \to {}^{128}$Te(0_1^+), and 0.255 for the β^- decay ^{128}I$(1_1^+) \to {}^{128}$Xe(0_1^+).

As can be seen from Fig. 14(b), the $\log ft$ values obtained within the mapped and phenomenological approaches for the ^{A}Rh$(1_1^+) \to {}^A$Pd(2_1^+) decay differ considerably. The difference between the two calculations is especially large at $A = 110$ and 116. One sees from Fig. 15(b), that the GT matrix element $M(\mathrm{GT}; 1_1^+ \to 2_1^+)$ for the ^{116}Rh decay in the phenomenological calculations is much larger in magnitude than the one obtained within the mapped approach, with the largest contribution coming from the term associated with the $\nu 0g_{7/2} - \pi 0g_{9/2}$ coupling. Generally, the predicted $\log ft$ values for the $1_1^+ \to 2_1^+$ β^- decay, both within the mapped and phenomenological schemes, increase with A (or N). This is

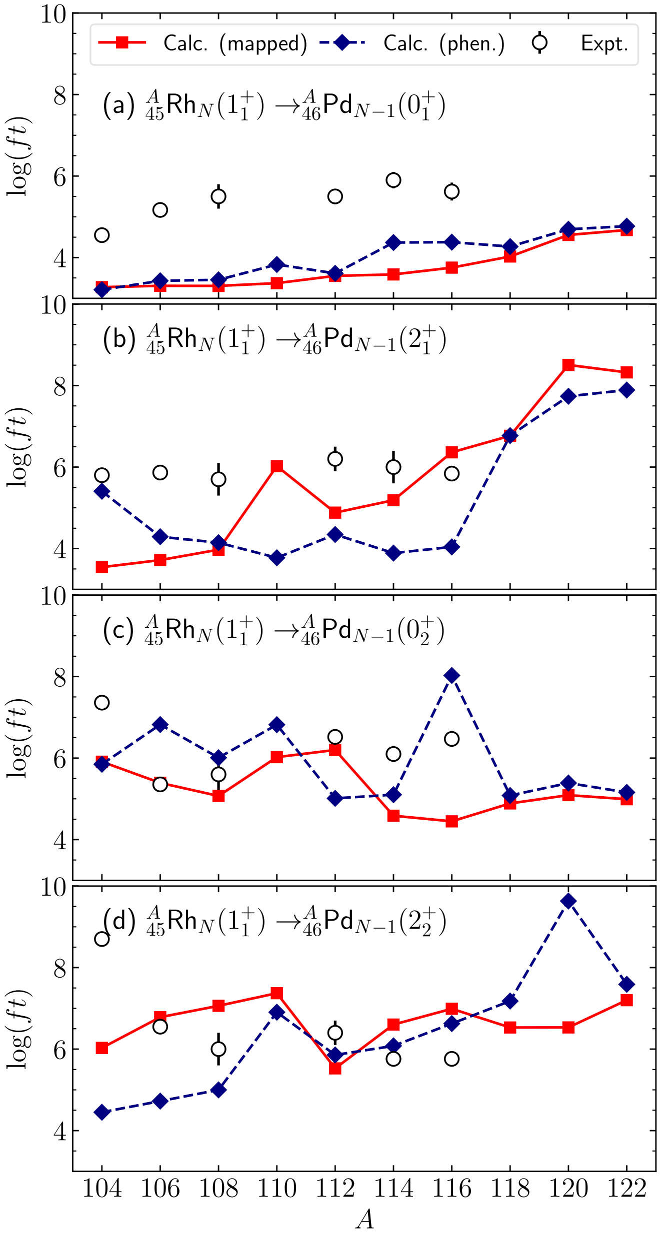

FIG. 14. The same as in Fig. 13, but for the β^- decays (a) $1^+_1 \to 0^+_1$, (b) $1^+_1 \to 2^+_1$, (c) $1^+_1 \to 0^+_2$, and (d) $1^+_1 \to 2^+_2$ from the even-A Rh into Pd nuclei.

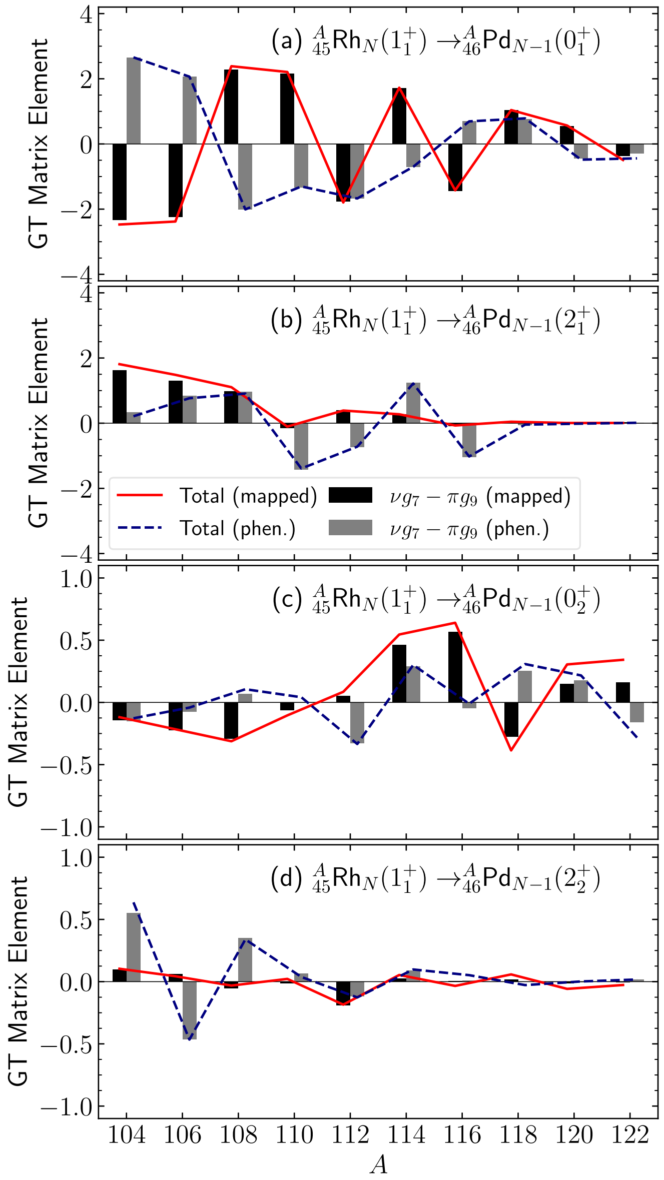

FIG. 15. Reduced matrix elements of the $\nu 0g_{7/2} - \pi 0g_{9/2}$ terms in the GT transition operators, and total GT matrix elements for the β^- decays (a) $1^+_1 \to 0^+_1$, (b) $1^+_1 \to 2^+_1$, (c) $1^+_1 \to 0^+_2$, and (d) $1^+_1 \to 2^+_2$ of the even-A Rh, resulting from the mapped and phenomenological calculations.

due to the fact that the pair configuration $[\nu 0g_{7/2} \otimes \pi 0g_{9/2}]^{(J)}$ gradually becomes less important in the 1^+_1 wave function of the even-A Rh for larger A [see Fig. 12(a)].

For the ${}^{A}\mathrm{Rh}(1^+_1) \to {}^{A}\mathrm{Pd}(0^+_2)$ decay, the $\log ft$ values predicted within the mapped and phenomenological approaches are similar. The most notable difference occurs at $A = 116$, with the mapped $\log ft$ value being nearly half the phenomenological one. This is a consequence of the fact that in the mapped GT matrix element $M(\mathrm{GT}; 1^+_1 \to 0^+_2)$ associated with the ^{116}Rh decay, the component of Eq. (27) is an order of magnitude larger than the one in the phenomenological calculations [see Fig. 15(c)]. In addition, the computed $\log ft$ values for the $1^+_1 \to 0^+_2$ decay are larger than those for the $1^+_1 \to 0^+_1$ decay because the matrix elements of the components involving the coupling $\nu 0g_{7/2} - \pi 0g_{9/2}$ in the $M(\mathrm{GT}; 1^+_1 \to 0^+_2)$ strength are smaller in magnitude than those in the $M(\mathrm{GT}; 1^+_1 \to 0^+_1)$ one.

The $\log ft$ values corresponding to the ${}^{A}\mathrm{Rh}(1^+_1) \to {}^{A}\mathrm{Pd}(2^+_2)$ decay are depicted in Fig. 14(d). Both the mapped and phenomenological calculations largely underestimate the measured value at $A = 104$. However, the results obtained with both schemes reproduce the experimental trend reasonably well for $108 \leqslant A \leqslant 116$. As can be seen from Fig. 15(d), the difference between the mapped and phenomenological results for $104 \leqslant A \leqslant 108$ is due to the difference between the matrix elements for the components $\nu 0g_{7/2} - \pi 0g_{9/2}$ in both schemes, with the mapped matrix elements being an order of magnitude smaller than the phenomenological ones.

For the sake of completeness, Table VI compares the predicted and experimental [70] $\log ft$ values for the β^- decays of the even-A Rh isotopes. Cases other than those already discussed above are considered in the table. As compared with the ground-state-to-ground-state decay $1_1^+ \to 0_1^+$, the ft values for the decays of the 1_1^+ state into non-yrast 1^+ and 2^+ states, and the $\log ft$ values for the $5_1^+ \to I_f$ and $6_1^+ \to I_f$ decays are calculated to be large. Note that the predicted $\log ft$ values for the decays ${}^{104}\mathrm{Rh}(5_1^+) \to {}^{104}\mathrm{Pd}(4_1^+)$ and ${}^{108}\mathrm{Rh}(5_1^+) \to {}^{108}\mathrm{Pd}(6_1^+)$ are rather close to the experimental ones.

VII. CONCLUSIONS

In this paper, the low-energy collective states and β decays for even and odd-mass neutron-rich Rh and Pd isotopes have been studied using a mapping framework based on the Gogny-EDF and the particle-boson coupling scheme. The constrained HFB has been employed to provide microscopic input to the mapping procedure. Such an input consists of potential-energy surfaces as functions of the (β, γ) shape degrees of freedom for the even-even ${}^{104-124}\mathrm{Pd}$ isotopes. The IBM-2 Hamiltonian, used to describe even-even core nuclei, has been determined by mapping the Gogny-D1M HFB fermionic potential-energy surfaces onto the corresponding bosonic surfaces. The microscopic mean-field calculations also provided single-particle energies for the odd systems. Those represent essential building blocks of the boson-fermion interactions for the neighboring odd-A and odd-odd nuclei as well as for the GT and Fermi transition operators. The strength parameters of the boson-fermion and residual neutron-proton interactions were fit to low-energy data for the odd-A and odd-odd systems.

The Gogny-HFB (β, γ) potential-energy surfaces obtained for even-even Pd isotopes point towards a transition from prolate deformed (${}^{104-108}\mathrm{Pd}$) to γ-soft (${}^{110-116}\mathrm{Pd}$), and to nearly spherical shapes (${}^{118-124}\mathrm{Pd}$). The low-energy excitation spectra and $B(E2)$ transition strengths resulting from the diagonalization of the mapped IBM-2 Hamiltonian reproduced the experimental trends reasonably well and reflect, to a large extent, the structural evolution of the ground-state shapes predicted at the mean-field level. The excitation energies obtained for the low-lying positive-parity levels in the odd-A Pd and Rh, and even-A Rh nuclei also exhibit signatures of this structural evolution. Within this context, a notable example is the change in the ground-state spin from ${}^{113}\mathrm{Pd}$ to ${}^{115}\mathrm{Pd}$. The computed $\log ft$ values for the β^- decays of the odd- and even-A Rh into Pd nuclei have been shown to be sensitive to the nature of the wave functions of the parent and daughter nuclei. They also reflect the rapid structural evolution along the considered isotopic chains. The $\log ft$ values for the odd-A Rh decay have been predicted to be larger than the experimental ones for $A \lesssim 109$. This could be traced back to the structure of the IBFM-2 wave functions for the odd-A daughter (Pd) nuclei. Furthermore, it has been shown that, for the even-A Rh decay, the neutron-proton pair components $[\nu 0g_{7/2} \otimes \pi 0g_{9/2}]^{(J)}$ play a key role in the GT transition matrix elements and are

TABLE VI. The same as in Table V, but for the β^- decays from even-A Rh to Pd nuclei.

		Calc.		
Decay	$I_i \to I_f$	Mapped	Phen.	Expt.
${}^{104}\mathrm{Rh} \to {}^{104}\mathrm{Pd}$	$1_1^+ \to 0_1^+$	3.27	3.21	4.55(1)
	$1_1^+ \to 2_1^+$	3.54	5.41	5.80(1)
	$1_1^+ \to 0_2^+$	5.91	5.85	7.36(2)
	$1_1^+ \to 2_2^+$	6.03	4.45	8.7(1)
	$1_1^+ \to 0_3^+$	6.42	6.05	5.5(1)
	$1_1^+ \to 2_3^+$	5.24	4.72	6.3(1)
	$5_1^+ \to 4_1^+$	7.26	8.30	7.3(1)
	$5_1^+ \to 4_2^+$	8.45	7.59	6.1(1)
	$5_1^+ \to 4_3^+$	8.06	8.04	6.2(1)
	$5_1^+ \to 4_4^+$	8.59	8.57	5.8(1)
${}^{106}\mathrm{Rh} \to {}^{106}\mathrm{Pd}$	$1_1^+ \to 0_1^+$	3.31	3.43	5.168(7)
	$1_1^+ \to 2_1^+$	3.72	4.29	5.865(17)
	$1_1^+ \to 2_2^+$	6.78	4.72	6.55(7)
	$1_1^+ \to 0_2^+$	5.39	6.82	5.354(19)
	$1_1^+ \to 2_3^+$	5.15	4.58	5.757(17)
${}^{108}\mathrm{Rh} \to {}^{108}\mathrm{Pd}$	$1_1^+ \to 0_1^+$	3.31	3.45	5.5(3)
	$1_1^+ \to 2_1^+$	3.97	4.14	5.7(4)
	$1_1^+ \to 2_2^+$	7.06	5.00	6.0(4)
	$1_1^+ \to 0_2^+$	5.07	6.01	5.6(4)
	$5_1^+ \to 6_1^+$	7.72	7.44	6.8(3)
	$5_1^+ \to 4_2^+$	8.28	7.00	4.84(9)[a]
	$5_1^+ \to 5_1^+$	9.59	8.35	4.84(9)[a]
	$5_1^+ \to 6_2^+$	9.30	9.42	4.84(9)[a]
${}^{110}\mathrm{Rh} \to {}^{110}\mathrm{Pd}$	$6_1^+ \to 6_1^+$	8.29	8.26	6.38(13)
	$6_1^+ \to 6_2^+$	9.57	8.95	7.1(4)
	$6_1^+ \to 5_1^+$	9.16	8.69	6.34(25)
${}^{112}\mathrm{Rh} \to {}^{112}\mathrm{Pd}$	$1_1^+ \to 0_1^+$	3.55	3.61	≈5.5
	$1_1^+ \to 2_1^+$	4.88	4.35	6.2(3)
	$1_1^+ \to 2_2^+$	5.53	5.86	6.4(3)
	$1_1^+ \to 0_2^+$	6.20	5.01	6.52(6)
	$1_1^+ \to 0_3^+$	7.48	6.36	6.88(9)[b]
	$1_1^+ \to 1_1^+$	7.74	5.66	6.88(9)[b]
	$1_1^+ \to 2_3^+$	5.83	5.39	6.88(9)[b]
	$1_1^+ \to 2_3^+$	5.83	5.39	6.97(22)
	$1_1^+ \to 2_3^+$	5.83	5.39	6.50(7)
	$6_1^+ \to 6_1^+$	8.75	8.80	6.52[c]
	$6_1^+ \to 5_1^+$	8.96	10.34	6.54
	$6_1^+ \to 6_2^+$	9.15	8.82	6.88
${}^{114}\mathrm{Rh} \to {}^{114}\mathrm{Pd}$	$1_1^+ \to 0_1^+$	3.59	4.37	5.9(2)
	$1_1^+ \to 2_1^+$	5.19	3.89	6.0(4)
	$1_1^+ \to 2_2^+$	6.60	6.08	5.7(2)
	$1_1^+ \to 0_2^+$	4.59	5.10	6.1(2)
	$1_1^+ \to 2_3^+$	5.57	5.28	6.1(2)
${}^{116}\mathrm{Rh} \to {}^{116}\mathrm{Pd}$	$1_1^+ \to 0_1^+$	3.75	4.38	5.62(22)
	$1_1^+ \to 2_1^+$	6.36	4.04	5.84(18)
	$1_1^+ \to 2_2^+$	6.99	6.63	5.76(19)
	$1_1^+ \to 0_2^+$	4.45	8.03	6.47(20)
	$1_1^+ \to 0_3^+$	5.29	8.60	6.36(19)
	$1_1^+ \to 2_3^+$	5.05	5.00	6.81(21)

[a] $4^+, 5^+, 6^+$ level at 2864 keV.

[b] $(0, 1, 2)^+$ level at 1140 keV.

[c] $\log ft$ values should be considered approximate [70].

responsible for the too small log ft values for the $^A\mathrm{Rh}(1_1^+) \rightarrow {}^A\mathrm{Pd}(0_1^+)$ decay with respect to the experimental data.

The results of the mapped calculations have been compared with conventional IBM-2 calculations in which the parameters for the boson Hamiltonian have been fit to the experiment. The mapped and phenomenological IBM-2 excitation spectra for even-even, odd-A, and odd-odd systems are similar. However, the two sets of calculations differ in their predictions for electromagnetic and β-decay properties of the odd-nucleon systems.

The results obtained in this study could be considered a plausible step towards a consistent simultaneous description of the low-lying states and β-decay properties of atomic nuclei. However, the difference between the predicted and experimental β-decay log ft values might require additional refinements of the employed theoretical framework. In particular, the small log ft values obtained suggest that the role of the effective axial-vector coupling constant g_A should be further studied in future calculations. The $g_{A,\mathrm{eff}}$ values extracted in this work from the comparison with the experimental data turned out to be by a factor 7–8 smaller than the free nucleon value. This large quenching indicates deficiencies in the model space of the calculations or of the theoretical procedure itself. Investigation along these lines is in progress and will be reported elsewhere.

ACKNOWLEDGMENTS

This work is financed within the Tenure Track Pilot Programme of the Croatian Science Foundation and the École Polytechnique Fédérale de Lausanne, and Project No. TTP-2018-07-3554 Exotic Nuclear Structure and Dynamics, with funds of the Croatian-Swiss Research Programme. The work of L.M.R. is supported by the Spanish Ministry of Economy and Competitiveness (MINECO) Grant No. PGC2018-094583-B-I00.

[1] S. Nishimura, Z. Li, H. Watanabe, K. Yoshinaga, T. Sumikama, T. Tachibana, K. Yamaguchi, M. Kurata-Nishimura, G. Lorusso, Y. Miyashita, A. Odahara, H. Baba, J. S. Berryman, N. Blasi, A. Bracco, F. Camera, J. Chiba, P. Doornenbal, S. Go, T. Hashimoto *et al.*, Phys. Rev. Lett. **106**, 052502 (2011).

[2] G. Lorusso, S. Nishimura, Z. Y. Xu, A. Jungclaus, Y. Shimizu, G. S. Simpson, P.-A. Söderström, H. Watanabe, F. Browne, P. Doornenbal, G. Gey, H. S. Jung, B. Meyer, T. Sumikama, J. Taprogge, Z. Vajta, J. Wu, H. Baba, G. Benzoni, K. Y. Chae *et al.*, Phys. Rev. Lett. **114**, 192501 (2015).

[3] M. Quinn, A. Aprahamian, J. Pereira, R. Surman, O. Arndt, T. Baumann, A. Becerril, T. Elliot, A. Estrade, D. Galaviz, T. Ginter, M. Hausmann, S. Hennrich, R. Kessler, K.-L. Kratz, G. Lorusso, P. F. Mantica, M. Matos, F. Montes, B. Pfeiffer *et al.*, Phys. Rev. C **85**, 035807 (2012).

[4] F. T. Avignone, S. R. Elliott, and J. Engel, Rev. Mod. Phys. **80**, 481 (2008).

[5] P. Navrátil and J. Dobes, Phys. Rev. C **37**, 2126 (1988).

[6] F. Dellagiacoma and F. Iachello, Phys. Lett. B **218**, 399 (1989).

[7] N. Yoshida, L. Zuffi, and S. Brant, Phys. Rev. C **66**, 014306 (2002).

[8] S. Brant, N. Yoshida, and L. Zuffi, Phys. Rev. C **70**, 054301 (2004).

[9] N. Yoshida and F. Iachello, Prog. Theor. Exp. Phys. **2013**, 043D01 (2013).

[10] E. Mardones, J. Barea, C. E. Alonso, and J. M. Arias, Phys. Rev. C **93**, 034332 (2016).

[11] K. Nomura, R. Rodríguez-Guzmán, and L. M. Robledo, Phys. Rev. C **101**, 024311 (2020).

[12] K. Nomura, R. Rodríguez-Guzmán, and L. M. Robledo, Phys. Rev. C **101**, 044318 (2020).

[13] J. Ferretti, J. Kotila, R. I. Magana Vsevolodovna, and E. Santopinto, Phys. Rev. C **102**, 054329 (2020).

[14] K. Nomura, Phys. Rev. C **105**, 044306 (2022).

[15] R. Álvarez-Rodríguez, P. Sarriguren, E. Moya de Guerra, L. Pacearescu, A. Faessler, and F. Šimkovic, Phys. Rev. C **70**, 064309 (2004).

[16] P. Sarriguren, Phys. Rev. C **91**, 044304 (2015).

[17] J. M. Boillos and P. Sarriguren, Phys. Rev. C **91**, 034311 (2015).

[18] P. Pirinen and J. Suhonen, Phys. Rev. C **91**, 054309 (2015).

[19] F. Šimkovic, V. Rodin, A. Faessler, and P. Vogel, Phys. Rev. C **87**, 045501 (2013).

[20] M. T. Mustonen and J. Engel, Phys. Rev. C **93**, 014304 (2016).

[21] J. T. Suhonen, Front. Phys. **5**, 55 (2017).

[22] A. Ravlić, E. Yüksel, Y. F. Niu, and N. Paar, Phys. Rev. C **104**, 054318 (2021).

[23] F. Minato, T. Marketin, and N. Paar, Phys. Rev. C **104**, 044321 (2021).

[24] K. Langanke and G. Martínez-Pinedo, Rev. Mod. Phys. **75**, 819 (2003).

[25] E. Caurier, G. Martínez-Pinedo, F. Nowack, A. Poves, and A. P. Zuker, Rev. Mod. Phys. **77**, 427 (2005).

[26] S. Yoshida, Y. Utsuno, N. Shimizu, and T. Otsuka, Phys. Rev. C **97**, 054321 (2018).

[27] T. Suzuki, S. Shibagaki, T. Yoshida, T. Kajino, and T. Otsuka, Astrophys. J. Lett. **859**, 133 (2018).

[28] A. Kumar, P. C. Srivastava, J. Kostensalo, and J. Suhonen, Phys. Rev. C **101**, 064304 (2020).

[29] F. Iachello and A. Arima, *The Interacting Boson Model* (Cambridge University Press, Cambridge, 1987).

[30] F. Iachello and O. Scholten, Phys. Rev. Lett. **43**, 679 (1979).

[31] F. Iachello and P. Van Isacker, *The Interacting Boson-Fermion Model* (Cambridge University Press, Cambridge, 1991).

[32] S. Brant, V. Paar, and D. Vretenar, Z. Phys. A: At. Nucl. (1975) **319**, 355 (1984).

[33] P. Ring and P. Schuck, *The Nuclear Many-Body Problem* (Springer, Berlin, 1980).

[34] S. Goriely, S. Hilaire, M. Girod, and S. Péru, Phys. Rev. Lett. **102**, 242501 (2009).

[35] J. Decharge, M. Girod, and D. Gogny, Phys. Lett. B **55**, 361 (1975).

[36] L. M. Robledo, T. R. Rodríguez, and R. R. Rodríguez-Guzmán, J. Phys. G **46**, 013001 (2019).

[37] P. Van Isacker and G. Puddu, Nucl. Phys. A **348**, 125 (1980).

[38] M. Bender, P.-H. Heenen, and P.-G. Reinhard, Rev. Mod. Phys. **75**, 121 (2003).

[39] D. Vretenar, A. V. Afanasjev, G. A. Lalazissis, and P. Ring, Phys. Rep. **409**, 101 (2005).

[40] T. Nikšić, D. Vretenar, and P. Ring, Prog. Part. Nucl. Phys. **66**, 519 (2011).

[41] J. F. Berger, M. Girod, and D. Gogny, Nucl. Phys. A **428**, 23 (1984).

[42] M. Borrajo and J. L. Egido, Eur. Phys. J. A **52**, 277 (2016).

[43] P. E. Garrett, T. R. Rodríguez, A. Diaz Varela, K. L. Green, J. Bangay, A. Finlay, R. A. E. Austin, G. C. Ball, D. S. Bandyopadhyay, V. Bildstein, S. Colosimo, D. S. Cross, G. A. Demand, P. Finlay, A. B. Garnsworthy, G. F. Grinyer, G. Hackman, B. Jigmeddorj, J. Jolie, W. D. Kulp *et al.*, Phys. Rev. C **101**, 044302 (2020).

[44] M. Siciliano, I. Zanon, A. Goasduff, P. R. John, T. R. Rodríguez, S. Péru, I. Deloncle, J. Libert, M. Zielińska, D. Ashad, D. Bazzacco, G. Benzoni, B. Birkenbach, A. Boso, T. Braunroth, M. Cicerchia, N. Cieplicka-Oryńczak, G. Colucci, F. Davide, G. de Angelis *et al.*, Phys. Rev. C **102**, 014318 (2020).

[45] M. Siciliano, J. J. Valiente-Dobón, A. Goasduff, T. R. Rodríguez, D. Bazzacco, G. Benzoni, T. Braunroth, N. Cieplicka-Oryńczak, E. Clément, F. C. L. Crespi, G. de France, M. Doncel, S. Ertürk, C. Fransen, A. Gadea, G. Georgiev, A. Goldkuhle, U. Jakobsson, G. Jaworski, P. R. John *et al.*, Phys. Rev. C **104**, 034320 (2021).

[46] R. Rodríguez-Guzmán, Y. M. Humadi, and L. M. Robledo, J. Phys. G **48**, 015103 (2021).

[47] R. Rodríguez-Guzmán and L. M. Robledo, Phys. Rev. C **103**, 044301 (2021).

[48] R. Rodríguez-Guzmán, L. M. Robledo, K. Nomura, and N. C. Hernandez, J. Phys. G **49**, 015101 (2022).

[49] K. Nomura, R. Rodríguez-Guzmán, L. M. Robledo, and N. Shimizu, Phys. Rev. C **86**, 034322 (2012).

[50] K. Nomura, R. Rodríguez-Guzmán, and L. M. Robledo, Phys. Rev. C **87**, 064313 (2013).

[51] K. Nomura, R. Rodríguez-Guzmán, and L. M. Robledo, Phys. Rev. C **94**, 044314 (2016).

[52] K. Nomura, R. Rodríguez-Guzmán, and L. M. Robledo, Phys. Rev. C **92**, 014312 (2015).

[53] K. Nomura, R. Rodríguez-Guzmán, Y. M. Humadi, L. M. Robledo, and J. E. García-Ramos, Phys. Rev. C **102**, 064326 (2020).

[54] K. Nomura, R. Rodríguez-Guzmán, L. M. Robledo, and J. E. García-Ramos, Phys. Rev. C **103**, 044311 (2021).

[55] K. Nomura, R. Rodríguez-Guzmán, L. M. Robledo, J. E. García-Ramos, and N. C. Hernández, Phys. Rev. C **104**, 044324 (2021).

[56] K. Nomura, R. Rodríguez-Guzmán, and L. M. Robledo, Phys. Rev. C **104**, 054320 (2021).

[57] T. Otsuka, A. Arima, and F. Iachello, Nucl. Phys. A **309**, 1 (1978).

[58] T. Otsuka, A. Arima, F. Iachello, and I. Talmi, Phys. Lett. B **76**, 139 (1978).

[59] O. Scholten, Prog. Part. Nucl. Phys. **14**, 189 (1985).

[60] S. Brant and V. Paar, Z. Phys. A **329**, 151 (1988).

[61] A. Bohr and B. R. Mottelson, *Nuclear Structure* (Benjamin, New York, 1975).

[62] J. N. Ginocchio and M. W. Kirson, Nucl. Phys. A **350**, 31 (1980).

[63] K. Nomura, N. Shimizu, and T. Otsuka, Phys. Rev. Lett. **101**, 142501 (2008).

[64] K. Nomura, N. Shimizu, and T. Otsuka, Phys. Rev. C **81**, 044307 (2010).

[65] K. Nomura, T. Nikšić, and D. Vretenar, Phys. Rev. C **93**, 054305 (2016).

[66] K. Nomura, R. Rodríguez-Guzmán, and L. M. Robledo, Phys. Rev. C **96**, 064316 (2017).

[67] K. Nomura, R. Rodríguez-Guzmán, and L. M. Robledo, Phys. Rev. C **99**, 034308 (2019).

[68] F. Dellagiacoma, Ph.D. thesis, Yale University, 1988 (unpublished).

[69] F. Iachello, Phys. Rev. Lett. **85**, 3580 (2000).

[70] Brookhaven National Nuclear Data Center, http://www.nndc.bnl.gov.

[71] J. Kurpeta *et al.*, Phys. Rev. C **98**, 024318 (2018).

[72] J. Kurpeta *et al.*, Phys. Rev. C **105**, 034316 (2022).

[73] N. Stone, At. Data Nucl. Data Tables **90**, 75 (2005).

[74] J. Arias, C. Alonso, and M. Lozano, Nucl. Phys. A **466**, 295 (1987).